Direct numerical simulation of particle alignment in viscoelastic fluids

Please check the document version of this publication:

• A submitted manuscript is the version of the article upon submission and before peer-review. There can be important differences between the submitted version and the official published version of record. People interested in the research are advised to contact the author for the final version of the publication, or visit the DOI to the publisher's website.
• The final author version and the galley proof are versions of the publication after peer review.
• The final published version features the final layout of the paper including the volume, issue and page numbers.

Link to publication

Direct numerical simulation of particle alignment in viscoelastic fluids

N.O. Jaensson[*1,2], M.A. Hulsen[1], and P.D. Anderson[1]

[1]Department of Mechanical Engineering, Eindhoven University of Technology,

P.O. Box 513, 5600 MB Eindhoven, The Netherlands

[2]Dutch Polymer Institute (DPI), P.O. Box 902, 5600 AX Eindhoven, The Netherlands

July 18, 2016

Abstract

Rigid particles suspended in viscoelastic fluids under shear can align in string-like structures in the flow direction. Although this phenomenon was first reported almost four decades ago by Michele et al. [1], the exact mechanism of particle alignment is not completely understood. Initially, it was believed that normal stress differences are responsible for the alignment of particles, but recent experimental work by van Loon et al. [2] showed particle alignment in a shear-thinning fluid without significant normal stress differences.

To unravel the phenomenon of particle alignment, we present for the first time 3D direct numerical simulations of the alignment of two and three rigid, non-Brownian particles in a viscoelastic shear flow, with the shear rate denoted by $\dot{\gamma}$. The equations are solved on moving, boundary-fitted meshes, which are locally refined to accurately describe the polymer stresses around and in between the particles. A small minimal gap size between the particles is introduced. The Giesekus model, with a relaxation time λ, is used for the viscoelastic fluid, and the effect of the Weissenberg number $\mathrm{Wi} = \lambda\dot{\gamma}$, shear thinning parameter α and ratio between the solvent viscosity and zero-shear viscosity β is investigated.

The numerical method allows for the detailed investigation of particles interacting in viscoelastic flows. Alignment of two and three particles is observed in the simulations. Morphology plots were created for various values of α, β and Wi. Alignment is mainly governed

[*]n.o.jaensson@tue.nl

by the value of the elasticity parameter S, defined as half of the ratio between the first normal stress difference and shear stress of the suspending fluid. Alignment appears to occur above a critical value of S, which decreases with increasing α, thus shear thinning promotes alignment. Furthermore, three particles align at lower S than two particles. Finally, simulations were performed in a shear-thinning Carreau fluid, where we never observed alignment of the particles. These results lead us to the conclusion that the presence of normal stress differences is essential for particle alignment to occur, although it is strongly promoted by shear thinning.

1 Introduction

The dynamics of non-Brownian particles in creeping flow has received a great deal of attention over the last century, starting with the classical work of Einstein on the rheology of dilute suspensions of rigid spheres [3, 4]. The majority of the theoretical, experimental, and numerical research has been on particles suspended in Newtonian fluids, e.g. see the reviews [5] and [6]. Recent work in this area is focused on the departure from Newtonian behavior of the suspension at high volume fractions, e.g. by including friction between particles [7–9].

Driven by the increasing use of polymer composites (e.g. a polymer matrix filled with rigid particles [10]), the investigation of the dynamics of rigid particles in viscoelastic fluids has recently seen an upsurge. See [11] and references therein for a recent review on this topic. Particles in viscoelastic fluids under creeping flow conditions have the tendency to migrate across streamlines [12, 13], which does not occur if the suspending fluid is Newtonian. It is believed that the migration is driven by gradients in normal stresses, and particles tend to migrate toward regions where normal stresses are lower, e.g. the outer cylinder in a wide-gap Couette device [14]. Another clear difference with Newtonian fluids is the tendency of spherical particles to align in string-like structures in flow direction, as was first reported in [1] for particles located between two flat plates that oscillate back and forth. Further work on the alignment of particles in viscoelastic shear flow was done both experimentally [2, 15, 16], analytically [17] and numerically in 2D [18–21] or in 3D using a mesoscopic approach, where the polymers are represented by discrete particles [22, 23]. Although several groups have been working on the simulation of 3D viscoelastic suspensions [24–27], to the best of the authors' knowledge, particle alignment has not been observed in 3D direct numerical simulations of rigid, spherical particles

in shear flow.

An interesting discrepancy exists between the experimental and numerical results: alignment is not observed in experiments using Boger fluids [2, 28, 29]. However, particle chains are observed in 2D simulations using Oldroyd-B fluids, which have a constant viscosity [18, 20, 21]. The lack of chaining in Boger fluids, combined with the observation of particle strings in shear-thinning fluids without significant normal stress differences, led van Loon et al. [2] to the conclusion that shear-thinning plays an essential role in the formation of particle strings. In this paper, 3D direct numerical simulations are presented of non-Brownian, rigid, spherical particles in viscoelastic fluids under shear. The finite element method is used on moving, boundary fitted meshes, which is an effective approach due to the availability of mesh generators that can efficiently mesh complicated 3D geometries [30]. We will systematically study the effect of the rheology of the suspending fluid on the alignment of two and three particles.

2 Problem statement

We consider non-Brownian, inertialess, mono-disperse particles of radius a in a shear flow, as depicted in Fig. 1. Due to the movement of the rigid top and bottom walls, a shear flow with an average shear rate of $\dot{\gamma} = 2U_{\mathrm{w}}/H$ is imposed, where U_{w} denotes the magnitude of the velocity of the walls. The fluids will be described as either Newtonian, viscoelastic or non-elastic but shear-thinning (Carreau), and the alignment of the particles will be investigated. It is assumed that the problem is symmetric in the xy-planes at $z = 0$ and $z = W/2$, and rotationally symmetric around the z-axis. Using these symmetries, it suffices to consider a quarter of the domain when three particles are simulated, whereas half of the domain is considered when two particles are simulated. This will explained in more detail in Section 4.
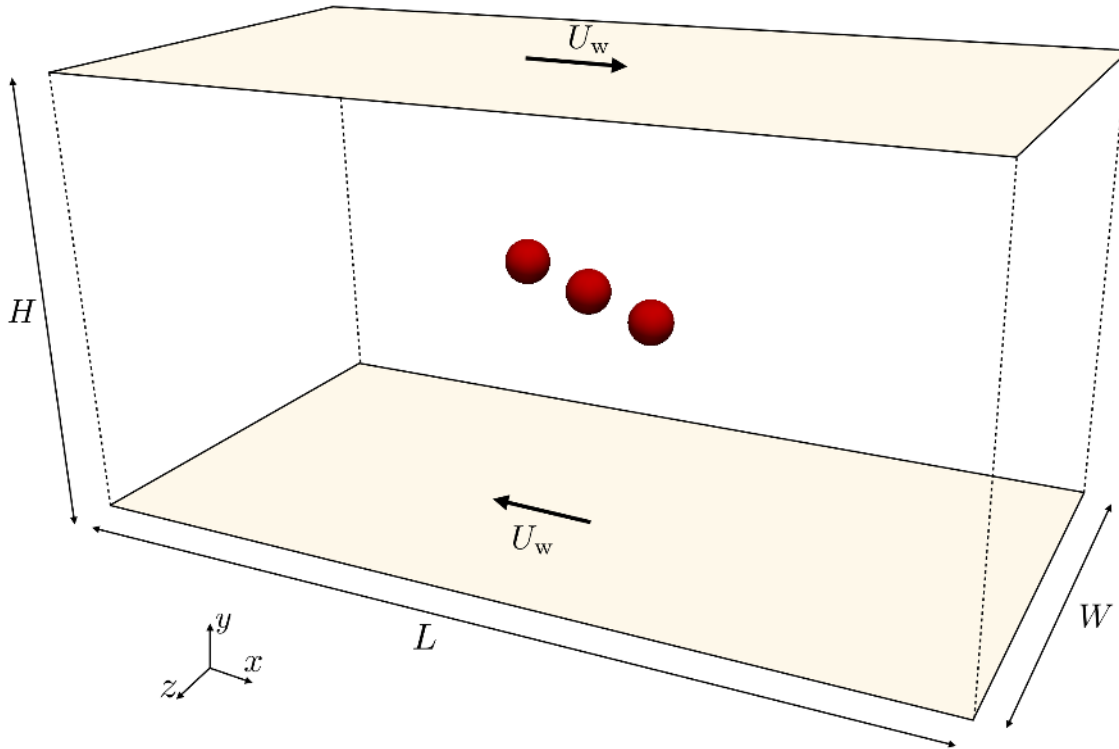
Fig. 1: The problem consists of rigid spheres in a shear flow. The domain is bounded in y-direction by rigid walls and periodicity is assumed in x-direction. For the z-direction, symmetry is assumed in the xy-planes at $z = 0$ and $z = W/2$ (the origin is located at the centroid of the rectangular box).

3   Governing equations

Assuming incompressible, inertialess flow, the balance of momentum and balance of mass are written as

$$-\nabla \cdot \boldsymbol{\sigma} = \boldsymbol{0}, \tag{1}$$

$$\nabla \cdot \boldsymbol{u} = 0, \tag{2}$$

where $\boldsymbol{\sigma}$ is the Cauchy stress tensor and $\boldsymbol{u}$ is the fluid velocity. The Cauchy stress can be decomposed in a pressure part, a Newtonian (solvent) part and a viscoelastic part:

$$\boldsymbol{\sigma} = -p\boldsymbol{I} + 2\eta_{\mathrm{s}}\boldsymbol{D} + \boldsymbol{\tau}, \tag{3}$$

where p is the pressure, $\boldsymbol{I}$ is the unit tensor, η_{s} is the Newtonian solvent viscosity, $\boldsymbol{D} = (\nabla\boldsymbol{u} + (\nabla\boldsymbol{u})^T)/2$ is the rate of deformation tensor, and $\boldsymbol{\tau}$ is the viscoelastic stress tensor. To model the

4

viscoelastic fluid, the Giesekus constitutive model will be used, which shows qualitatively correct rheological properties of a polymeric fluid (i.e. shear thinning viscosity, first and second normal stress differences, bounded extensional viscosity). Using the Giesekus constitutive model, the evolution of the viscoelastic stress is described by [31]:

$$\lambda \overset{\nabla}{\boldsymbol{\tau}} + \boldsymbol{\tau} + \frac{\lambda \alpha}{\eta_{\mathrm{p}}} \boldsymbol{\tau}^2 = 2\eta_{\mathrm{p}} \boldsymbol{D}, \tag{4}$$

where λ is the relaxation time, η_{p} is the polymer viscosity and α is the mobility, which controls the shear-thinning behavior of the fluid. The zero-shear viscosity of the fluid is given by $\eta_0 = \eta_{\mathrm{s}} + \eta_{\mathrm{p}}$. Furthermore, the upper convected derivative is defined as

$$\overset{\nabla}{()} = \frac{\mathrm{D}()}{\mathrm{D}t} - (\nabla \boldsymbol{u})^T \cdot () - () \cdot \nabla \boldsymbol{u}, \tag{5}$$

where $\mathrm{D}()/\mathrm{D}t$ denotes the material derivative. The evolution of the polymer stress, described by Eq. (4), can be rewritten to the equivalent

$$\boldsymbol{\tau} = G(\boldsymbol{c} - \boldsymbol{I}), \tag{6}$$

$$\lambda \overset{\nabla}{\boldsymbol{c}} + \boldsymbol{c} - \boldsymbol{I} + \alpha(\boldsymbol{c} - \boldsymbol{I})^2 = \boldsymbol{0}, \tag{7}$$

where $\boldsymbol{c}$ is the conformation tensor and $G = \eta_{\mathrm{p}}/\lambda$ is the polymer modulus. When supplemented with the proper boundary conditions, Eqs. (1), (2), (6) and (7) form a well-posed problem for the unknowns $\boldsymbol{u}$, p and $\boldsymbol{c}$.

Simulations will also be performed using a shear-thinning, viscous fluid which is modeled by the Carreau model with the viscosity at infinite shear rate set to zero, for which the Cauchy stress tensor is written as

$$\boldsymbol{\sigma} = -p\boldsymbol{I} + 2\eta(\dot{\gamma}_{\mathrm{e}})\boldsymbol{D}, \tag{8}$$

with

$$\eta(\dot{\gamma}_{\mathrm{e}}) = \frac{\eta_0}{(1 + (\lambda_{\mathrm{c}}\dot{\gamma}_{\mathrm{e}})^2)^{(1-n)/2}}, \tag{9}$$

where λ_{c} is a characteristic time, n is the power-law index and $\dot{\gamma}_{\mathrm{e}} = \sqrt{2\boldsymbol{D}:\boldsymbol{D}}$ is an "effective shear rate" (for simple shear: $\dot{\gamma}_{\mathrm{e}} = \dot{\gamma}$). Despite the presence of a characteristic time λ_{c}, there is no fluid memory in the Carreau model.

It is assumed that inertia of the particles can be neglected. Assuming no external forces and torques are imposed on the particles, this means that the particles are force- and torque-free:

$$\int_{\partial P_i} \boldsymbol{\sigma} \cdot \boldsymbol{n} \, dS = \boldsymbol{0}, \tag{10}$$

$$\int_{\partial P_i} (\boldsymbol{x} - \boldsymbol{X}_i) \times (\boldsymbol{\sigma} \cdot \boldsymbol{n}) \, dS = \boldsymbol{0}, \tag{11}$$

where $\boldsymbol{n}$ is the outwardly directed unit normal vector on the particle boundary ∂P_i and $\boldsymbol{X}_i = [X_i, Y_i, 0]$ denotes the location of the center point of the i-th particle. As will become clear in Section 3.1, initially an additional force is applied on the particle which is gradually removed in a short amount of time. In that case the force balance (Eq. (10)) becomes:

$$\int_{\partial P_i} \boldsymbol{\sigma} \cdot \boldsymbol{n} \, dS = \boldsymbol{F}_i, \tag{12}$$

where $\boldsymbol{F}_i = [F_{x,i}, F_{y,i}, 0]$ is the external force on the i-th particle. The z-component of the force and the position are set to zero due to symmetry considerations, as will be explained in Section 4.

The relationship between the position and velocity is described through a kinematic equation:

$$\frac{d\boldsymbol{X}_i}{dt} = \boldsymbol{U}_i, \tag{13}$$

where $\boldsymbol{U}_i = [U_{x,i}, U_{y,i}, 0]$ is the i-th particle translational velocity, where the z-component is zero due to symmetry. The orientation of the particles does not need updating due to the particles being spherical.

3.1 Boundary and initial conditions

In this section, the boundary and initial conditions are defined. In the numerical implementation only part of the box depicted in Fig. 1 is simulated. This approach greatly improves numerical efficiency, as was shown in [32] for a single rotating sphere.

3.1.1 Boundary conditions for two particles

For the problem of two particles, it is assumed that the particles move in the xy-plane, i.e. $\boldsymbol{X}_i = [X_i, Y_i, 0]$ for $i = 1 \ldots N$. Periodicity is assumed in x-direction and symmetry is assumed in the xy-planes at $z = 0$ and $z = W/2$. In this case, only half of the domain has to be meshed, an example of which is shown in Fig. 2. Assuming no-slip on the rigid boundaries yields for the velocity

$$\boldsymbol{u} = [U_{\mathrm{w}}, 0, 0] \qquad\qquad \text{on } \Gamma_6, \qquad (14)$$

$$\boldsymbol{u} = [-U_{\mathrm{w}}, 0, 0] \qquad\qquad \text{on } \Gamma_5, \qquad (15)$$

$$\boldsymbol{u} = \boldsymbol{U}_i + \boldsymbol{\omega}_i \times (\boldsymbol{x} - \boldsymbol{X}_i) \qquad\qquad \text{on } \partial P_i, \qquad (16)$$

where the particle velocity $\boldsymbol{U}_i$ and angular velocity $\boldsymbol{\omega}_i$ are such that the force balance (Eq. (10)) and torque balance (Eq. (11)) for the i-th particle are fulfilled. The plane symmetry in the xy-planes yields:

$$
\begin{array}{lll}
(t_x)_{\Gamma_2} = 0 & (t_y)_{\Gamma_2} = 0 & (u_z)_{\Gamma_2} = 0 \\[4pt]
(t_x)_{\Gamma_4} = 0 & (t_y)_{\Gamma_4} = 0 & (u_z)_{\Gamma_4} = 0,
\end{array}
\qquad (17)
$$

where t_x and t_y are the x- and y-component of the traction vector $\boldsymbol{t} = \boldsymbol{\sigma} \cdot \boldsymbol{m}$, where $\boldsymbol{m}$ is the outwardly directed unit normal vector on the boundary. Periodicity in x-direction yields the boundary conditions

$$
\begin{array}{lll}
(u_x)_{\Gamma_1} = (u_x)_{\Gamma_3} & (u_y)_{\Gamma_1} = (u_y)_{\Gamma_3} & (u_z)_{\Gamma_1} = (u_z)_{\Gamma_3} \\[4pt]
(t_x)_{\Gamma_1} = -(t_x)_{\Gamma_3} & (t_y)_{\Gamma_1} = -(t_y)_{\Gamma_3} & (t_z)_{\Gamma_1} = -(t_z)_{\Gamma_3} \\[4pt]
(c_{xx})_{\Gamma_1} = (c_{xx})_{\Gamma_3} & (c_{xy})_{\Gamma_1} = (c_{xy})_{\Gamma_3} & (c_{yy})_{\Gamma_1} = (c_{yy})_{\Gamma_3} \\[4pt]
(c_{zz})_{\Gamma_1} = (c_{zz})_{\Gamma_3} & (c_{xz})_{\Gamma_1} = (c_{xz})_{\Gamma_3} & (c_{yz})_{\Gamma_1} = (c_{yz})_{\Gamma_3}.
\end{array}
\qquad (18)
$$

In all simulations presented for two particles in Section 5, the problem is rotationally symmetric around the z-axis (with a rotation angle of $180°$). In principle, this would allow for the simulation of only a quarter of the domain. For practical reasons, we chose not to do that here.
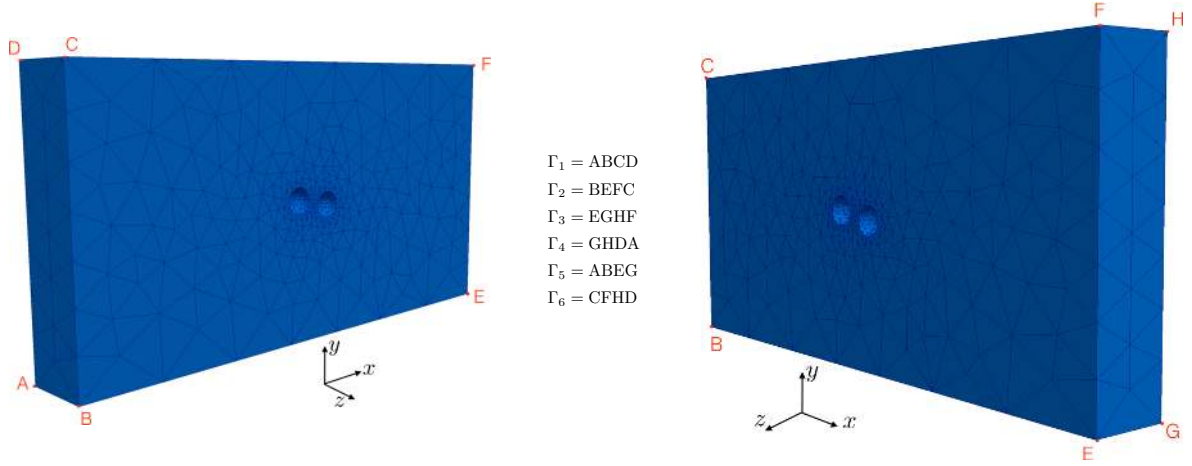
Fig. 2: Two views of a mesh used for two particles. Plane Γ_1 can be identified with Γ_3. These planes will be connected node-by-node using a collocation method, and are therefore meshed periodically. Note, that this mesh is for illustrative purposes and the meshes used in Section 5 are much more refined.
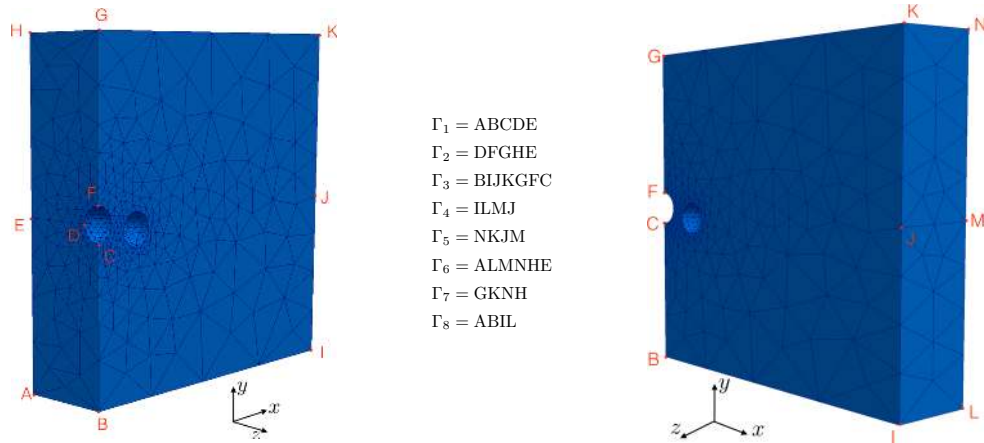

Fig. 3: Two views of a mesh used for three particles. Plane Γ_1 can be identified with Γ_2, and Γ_4 can be identified with Γ_5. These planes will be connected node-by-node using a collocation method, and the mesh is therefore generated such that Γ_1 and Γ_2 are symmetric in the line ED, and Γ_4 and Γ_5 are symmetric in the line JM. Note, that this mesh is for illustrative purposes and the meshes used in Section 5 are much more refined.

3.1.2 Boundary conditions for three particles

For the problem of three particles, it is assumed that the particles move in the xy-plane, i.e. $\boldsymbol{X}_i = [X_i, Y_i, 0]$ for $i = 1 \ldots N$. Periodicity is assumed in x-direction and symmetry is assumed in the xy-planes at $z = 0$ and $z = W/2$. Furthermore, the problem is assumed to be rotationally symmetric around the z-axis (with a rotation angle of $180°$): for the particle at $[X_i, Y_i, 0]$ with $X_i > 0$, there is an opposite particle at $-[X_i, Y_i, 0]$. The middle particle is located at the origin and is only free to rotate. Using these symmetries, only a quarter of the domain has to be meshed, an example of which is shown in Fig. 3. Assuming no-slip on the

rigid boundaries yields for the velocity

$$\boldsymbol{u} = [U_{\mathrm{w}}, 0, 0] \qquad\qquad \text{on } \Gamma_7, \qquad (19)$$

$$\boldsymbol{u} = [-U_{\mathrm{w}}, 0, 0] \qquad\qquad \text{on } \Gamma_8, \qquad (20)$$

$$\boldsymbol{u} = \boldsymbol{U}_i + \boldsymbol{\omega}_i \times (\boldsymbol{x} - \boldsymbol{X}_i) \qquad\qquad \text{on } \partial P_i. \qquad (21)$$

Since the middle particle is only free to rotate, $\boldsymbol{U}_i = \boldsymbol{0}$ in Eq. (21) for the middle particle. The plane symmetry in the xy-planes yields:

$$(t_x)_{\Gamma_3} = 0 \qquad (t_y)_{\Gamma_3} = 0 \qquad (u_z)_{\Gamma_3} = 0$$

$$(t_x)_{\Gamma_6} = 0 \qquad (t_y)_{\Gamma_6} = 0 \qquad (u_z)_{\Gamma_6} = 0, \qquad (22)$$

The rotational symmetry around the z-axis implies that the plane Γ_1 can be identified with plane Γ_2, after a rotation around the z-axis. Likewise, plane Γ_4 can be identified with plane Γ_5 after a rotation around the z-axis. By performing subsequent rotations around the z-axis, the periodic domain can be reconstructed. When performing this rotation on a local coordinate system, it is obvious that the x- and y-components of a vector described in that coordinate system reverse sign, whereas the z-component does not. When applying this to tensors, only the xz- and yz-components reverse sign. This yields the following boundary conditions connecting the planes Γ_1 and Γ_2:

$$(u_x)_{\Gamma_1} = -(u_x)_{\Gamma_2} \qquad (u_y)_{\Gamma_1} = -(u_y)_{\Gamma_2} \qquad (u_z)_{\Gamma_1} = \ \ (u_z)_{\Gamma_2}$$

$$(t_x)_{\Gamma_1} = \ \ (t_x)_{\Gamma_2} \qquad (t_y)_{\Gamma_1} = \ \ (t_y)_{\Gamma_2} \qquad (t_z)_{\Gamma_1} = -(t_z)_{\Gamma_2}$$

$$(c_{xx})_{\Gamma_1} = \ \ (c_{xx})_{\Gamma_2} \qquad (c_{xy})_{\Gamma_1} = \ \ (c_{xy})_{\Gamma_2} \qquad (c_{yy})_{\Gamma_1} = \ \ (c_{yy})_{\Gamma_2}$$

$$(c_{zz})_{\Gamma_1} = \ \ (c_{zz})_{\Gamma_2} \qquad (c_{xz})_{\Gamma_1} = -(c_{xz})_{\Gamma_2} \qquad (c_{yz})_{\Gamma_1} = -(c_{yz})_{\Gamma_2}, \qquad (23)$$

and similarly for Γ_4 and Γ_5. Note, that on the lines DE and JM the only possible solution for u_x, u_y, c_{xz} and c_{yz} is zero, which is thus prescribed as an essential boundary condition on these lines.

3.1.3 Initial conditions

Initial conditions are needed for the particle position and conformation tensor, which are denoted by

$$\boldsymbol{X}_i(t=0) = \boldsymbol{X}_{i,0} \tag{24}$$

$$\boldsymbol{c}(t=0) = \boldsymbol{c}_0. \tag{25}$$

Since we are interested in the interaction between particles in a flow where viscoelastic stresses have been "fully developed", imposing a stress-free state for the conformation tensor would not suffice. Instead, the initial conformation field is obtained by solving the full set of equations with the stress-free state as initial condition, but for torque-free particles with fixed location (i.e. $\boldsymbol{U}_i = 0$ in Eq. (16)). This problem is run for one relaxation time, which allows for the build-up of viscoelastic stresses. The resulting conformation tensor field $\boldsymbol{c}_0$ is used as an initial condition in the actual simulations. However, since $\boldsymbol{c}_0$ is determined with the particles being torque-free, but not necessarily force-free, a force will act on the particles, which would yield a sudden movement of the particles as they become freely-floating. This problem is tackled by determining the force on the rotating particles and imposing this force in the initial stage of the simulation, through $\boldsymbol{F}_i$ in Eq. (12). The force is then gradually released in one strain unit to let the particles become truly freely-floating.

4   Numerical method

4.1   Weak form

The boundary conditions on the particles given by Eq. (16) are implemented as constraints, with the particle angular and translational velocities as additional unknowns [33]. This approach introduces unknowns on the boundaries of the particles: the Lagrange multiplier $\boldsymbol{\lambda}_i$. The weak form of the momentum/mass balance (for the i-th particle that rotates and translates and is

subject to an external force $\boldsymbol{F}_i$) is written as: find $\boldsymbol{u}$, p, $\boldsymbol{U}_i$, $\boldsymbol{\omega}_i$ and $\boldsymbol{\lambda}_i$ such that

$$(\boldsymbol{D}_v, 2\eta_s \boldsymbol{D} + \boldsymbol{\tau}) - (\nabla \cdot \boldsymbol{v}, p) + \langle \boldsymbol{v} - (\boldsymbol{V}_i + \boldsymbol{\chi}_i \times (\boldsymbol{x} - \boldsymbol{X}_i), \boldsymbol{\lambda}_i \rangle_{\partial P_i} = \boldsymbol{V} \cdot \boldsymbol{F}_i \quad (26)$$

$$\left(q, \nabla \cdot \boldsymbol{u}\right) = 0 \quad (27)$$

$$\langle \boldsymbol{\mu}_i, \boldsymbol{u}_i - (\boldsymbol{U}_i + \boldsymbol{\omega}_i \times (\boldsymbol{x} - \boldsymbol{X}_i)) \rangle_{\partial P_i} = 0, \quad (28)$$

for all admissable test functions $\boldsymbol{v}$, q, $\boldsymbol{\chi}_i$, $\boldsymbol{V}_i$ and $\boldsymbol{\mu}_i$. Furthermore, $\boldsymbol{D}_v = \left(\nabla \boldsymbol{v} + (\nabla \boldsymbol{v})^T\right)/2$, the notation $(\cdot, \cdot)$ denotes a proper inner product on the fluid domain and $\langle \cdot, \cdot \rangle_{\partial P_i}$ is an inner product on ∂P_i.

The momentum and mass balance are solved first within a time step, with the polymer stress $\boldsymbol{\tau}$ determined by using a semi-implicit scheme as proposed in [34]. Using the log-conformation approach [35] and SUPG stabilization [36], the weak form of the evolution equation for conformation tensor (Eq. (7)) reads: find $\boldsymbol{s}$ such that

$$\left(\boldsymbol{d} + \tau(\boldsymbol{u} - \boldsymbol{u}_m) \cdot \nabla \boldsymbol{d}, \frac{D\boldsymbol{s}}{Dt} - \boldsymbol{g}\left((\nabla \boldsymbol{u})^T, \boldsymbol{s}\right)\right) = 0, \quad (29)$$

for all admissible test functions $\boldsymbol{d}$ and where $\boldsymbol{s} = \log \boldsymbol{c}$, the parameter τ is due to the SUPG stabilization and $\boldsymbol{u}_m$ denotes the mesh velocity, which will be introduced in Section 4.2. The reader is referred to [35] for details about the log-conformation approach and the expression for the function $\boldsymbol{g}$.

4.2 Discretization

To solve the velocity-pressure-conformation system as was presented in Section 3, the finite element method is used with tetrahedral $P_2 P_1 P_1$ elements for the velocity-pressure-conformation fields. Boundary fitted meshes are used, that move in time such that the mesh on the particle boundary follows the motion of the particle, whereas the remaining boundaries are stationary. Since the fluid is now described on a grid that moves with the material, but not in a Lagrangian manner, the arbitrary Lagrange Euler (ALE) formulation [37] is used. The moving grid is identified with the mesh, and the material derivative is rewritten to

$$\frac{D()}{Dt} = \frac{\partial()}{\partial t}\bigg|_{\boldsymbol{x}_m} + (\boldsymbol{u} - \boldsymbol{u}_m) \cdot (), \quad (30)$$

11

where the first term on the right hand side is the partial derivative at constant mesh coordinate $\boldsymbol{x}_{\mathrm{m}}$, i.e. the mesh derivative, and $\boldsymbol{u}_{\mathrm{m}}$ is the mesh velocity. A smooth displacement field for the entire mesh is found by solving a Laplace problem, similar to [37]. Once the mesh deformation becomes too large, remeshing is performed based on the position of the particles. Variables needed in the time integration, i.e. the conformation field at previous time steps, are projected onto the new mesh [37]. To obtain the new mesh at the previous instances in time, which is needed to find the mesh velocity, the mesh coordinates are projected as well [38]. Since the elements are aligned to the particle boundary, the inner product $\langle \cdot, \cdot \rangle_{\partial P_i}$ can be performed using a collocation method [33]. Meshes are generated using Gmsh [30].

Second-order time integration schemes are used for all time derivatives, and the momentum/mass balance and evolution equation for the conformation tensor are solved in two separate systems. To stabilize the evolution equation for the conformation tensor, SUPG [36] is applied and the log-conformation representation is used [35, 39]. Stabilization in the momentum balance is obtained by using an implicit-stress formulation, where a prediction of the conformation tensor is used in the momentum balance [34]. This approach allows for the simulations of fluids with a small or absent solvent contribution, and additional stabilization using DEVSS [40] is found not to be necessary.

At several stages within a time step, a system of equations has to be solved with a constant matrix but varying right-hand-side (e.g. the components of the conformation tensor). For these systems, a direct solver from the HSL library [41] is employed, which allows for the re-use of the LU-decomposition. The momentum balance is solved using a GMRES iterative solver with an ILUT preconditioner from the Sparskit library [42]. The mesh is moved in time, but the connectivity of the nodes remains unchanged. Therefore, the structure of the system matrix for the momentum balance is constant until a remeshing is performed, which allows for the re-use of the ILUT preconditioner. In most cases, the preconditioner could be used for a large number of timesteps, and only had to be rebuilt after a remeshing, significantly decreasing the computational time. To reduce fill-in when building the preconditioner, the nodes of the mesh are renumbered using MeTiS [43].

4.3 Minimal gap size between particles

As the particles come in close proximity, the fluid film in the gap between the particles becomes more difficult to describe. However, accurately resolving the stresses in this fluid film is essential to capture the complete interaction between particles. The approach taken here, is to locally refine the mesh in between the particles in an adaptive manner, ensuring there are always a minimum number of elements $(n_{\min})$ between the particle boundaries. For the velocity, which is interpolated using quadratic elements, this yields a minimum number of $2n_{\min} + 1$ nodes between particle boundaries. An example of such a locally refined mesh is shown in Fig. 4.
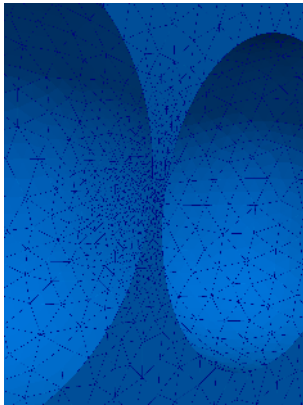

Fig. 4: Adaptive refinement ensures that there are always n_{min} elements in between the particles (here $n_{min} = 4$).

In the 2D simulations presented in [18, 21], it was shown that a fluid film of finite thickness remains in the gap between the particles. Accurately describing this fluid film using local mesh refinement was thus enough to keep the particles from coming into close proximity. In 3D, however, the simulations showed that the fluid films become much thinner for interacting spheres, yielding very large deformation rates in the gaps between the particles. As a result, large polymer stresses are generated, leading to a breakdown of the numerical scheme. As suggested in [37], a repulsive force, which can be interpreted as a consequence of the particle roughness, can help in keeping the particles apart. One option is to a-priori define a force as a function of the distance between the particles [33]. Another option is to determine this force iteratively in an optimization problem [44]. Our approach is different, and avoids an iterative procedure to find the repulsive force: the repulsive force is implicitly solved for, as an additional unknown in the system of equations. This is done by defining a minimal gap size between the particles, which will be denoted by $d_{\min}$. Once particles "step" into this region, their motion

is constrained such that the distance between the particles does not decrease further. We will explain this approach for two particles, but an arbitrary number of particles that are within a distance $d_{\min}$ could be constrained in this manner.
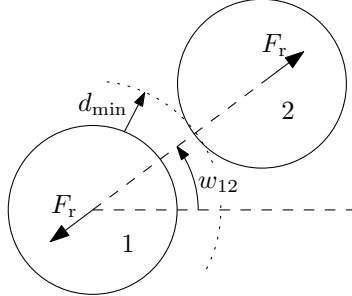

Fig. 5: Two particles are constrained such that the distance between the particle does not decrease. The angular velocity of the rotating rigid rod between the particle centers is denoted by w_{12}. The force F_r does not have to be specified a-priori, but follows from the constrained particle movement.

As the gap size between the particle boundaries becomes smaller than $d_{\min}$, which is typically chosen much smaller than the particle radius, the translational motion of the particles is constrained such that the distance between the particles does not decrease (one can imagine this as the particle centers being connected by rotating rigid rods). The translational velocity of one of the particles is removed as an unknown, but the angular velocity of the rigid rod connecting the particles, denoted by w_{12} in Fig. 5, is included as an unknown. Instead of using Eq. (16) for each particle, the velocity on the particle boundaries is now given by

$$\boldsymbol{u} = \boldsymbol{U}_1 + \boldsymbol{\omega}_1 \times (\boldsymbol{x} - \boldsymbol{X}_1) \qquad\qquad \text{on } \partial P_1 \qquad (31)$$

$$\boldsymbol{u} = \boldsymbol{U}_1 + \boldsymbol{w}_{12} \times (\boldsymbol{X}_2 - \boldsymbol{X}_1) + \boldsymbol{\omega}_2 \times (\boldsymbol{x} - \boldsymbol{X}_2) \qquad\qquad \text{on } \partial P_2, \qquad (32)$$

where it can be seen that the velocity on ∂P_2 depends on $\boldsymbol{U}_1$, which should be properly accounted for in the weak form given by Eqs. (26) and (28). The translational velocity of the second particle is given by $\boldsymbol{U}_2 = \boldsymbol{U}_1 + \boldsymbol{w}_{12} \times (\boldsymbol{X}_2 - \boldsymbol{X}_1)$. Note, that the component of $\boldsymbol{w}_{12} \times (\boldsymbol{X}_2 - \boldsymbol{X}_1)$ in the direction $\boldsymbol{X}_2 - \boldsymbol{X}_1$ disappears, effectively reducing the number of unknowns by one. We want to emphasize that the magnitude of the force between the particles, denoted by F_r, follows from the constrained movement of the particles and can be evaluated by summing the Lagrange multipliers on the particle boundary, and thus does not have to be specified a-priori. The repulsive force is directed along the vector connecting the particles, and from the sign of F_r it can be deduced if the particles want to move toward or away from each other. In the latter

case the constraint can be released and the normal weak form as given by Eqs. (26) to (28) is solved in the next time step. The influence of the size of $d_{\min}$ on the particle alignment will be investigated in Section 5.2.

The procedure can be extended to an arbitrary number of particles by including the translation velocity of one of the particles (denoted by $\boldsymbol{U}_1$, but the choice is arbitrary) and the angular velocities of the rotating rigid rods between the particles in the constraint. The translational velocities of all particles included in the constraint (those particles that are "connected" by a fluid layer of less than $d_{\min}$) now depend on $\boldsymbol{U}_1$ and the angular velocities of the rigid rods in between them, which should be properly accounted for when building the constraint equation. For a full 3D problem where the particles can move out-of-plane, many particles can be within $d_{\min}$, and geometrical constraints can yield dependencies between the rotations of the rigid rods, this is not a trivial task. For the simulation of three particles, the translational velocity of the middle particle is zero, thus $\boldsymbol{U}_1 = \boldsymbol{0}$ in Eqs. (31) and (32). Furthermore, Eq. (32) is implemented by rewriting $\boldsymbol{w}_{12} \times (\boldsymbol{X}_2 - \boldsymbol{X}_1) = U_2 \boldsymbol{\nu}$, where $\boldsymbol{\nu}$ is the unit vector perpendicular to $\boldsymbol{X}_2 - \boldsymbol{X}_1$, in the xy-plane.

5 Results

Simulations have been performed to investigate the string formation of two and three particles (with the symmetry assumptions as outlined in Section 4). In dimensionless form, the viscoelastic problem is described by the Weissenberg number, defined by $\mathrm{Wi} = \lambda \dot{\gamma}$, the mobility α which controls the shear-thinning behavior of the fluid, and the ratio between the solvent viscosity and the zero-shear viscosity, denoted by $\beta = \eta_{\mathrm{s}}/\eta_0$. Many of the results will be presented in terms of the angle between the line connecting the center points of the particles and the x-axis, which is denoted by θ and is defined in Fig. 6. For the two-particle problem, the particles are initially placed at an angle of $\theta = 10°$ with an initial distance between the center points of $3a$, yielding an initial distance a between the particle boundaries. Note, that in the very beginning of the simulations, a force is applied to the particles which is gradually removed in one strain unit, as explained in Section 3.1.3. The distance between the particle boundaries after one strain unit depends on the fluid parameters, but is around $a/2$. For the three-particle problem, the middle particle is initially placed at the origin, and will remain there during the entire simulation. The

outer particles are placed at an angle of $\theta = 10°$, with an initial distance between the center points of the middle and outer particles of $3a$. The size of the periodic domain as defined in Fig. 1 is set to $L = 80a$, $H = 40a$ and $W = 20a$, to ensure minimal wall and periodicity effects.
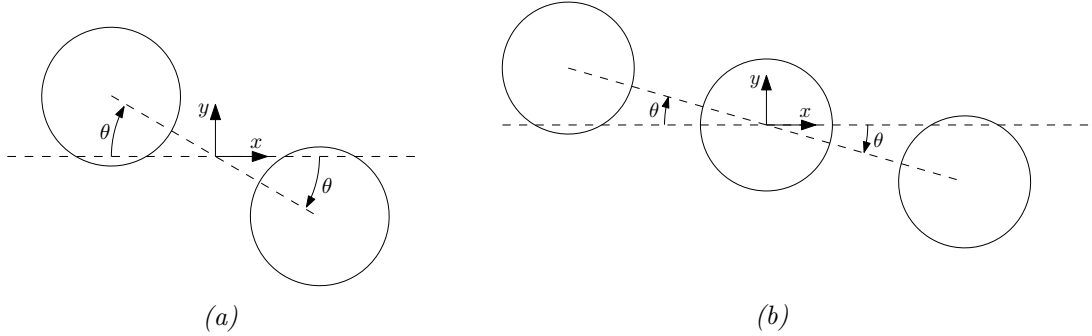

Fig. 6: The angle θ is defined as the angle between the x-axis and the line connecting the center points of the particles for the two-particle problem (a) and the three-particle problem (b).

5.1 Mesh and time convergence

We commence by investigating the mesh and time convergence, which will be done for the three-particle problem. Convergence was more difficult to obtain for high values of Wi and low values of α, β and $d_{\min}$. We study convergence for Wi $= 3$, $\alpha = 0.01$, $\beta = 0.1$ and $d_{\min} = 0.02$ in this section. Note, that $d_{\min}$ is normalized with the particle diameter $2a$ throughout this paper. The meshes are characterized by the number of elements on the equator of the particle (n_{part}) and the number of elements in between the particles ($n_{\min}$) as defined in Section 4.3. The base element size on and near the particles is thus $h_{\text{part}} = 2\pi a/n_{\text{part}}$, but smaller elements are used in between the particles to ensure $n_{\min}$ is satisfied. Far away from the particles, larger elements are used as shown in Fig. 3. Four different meshes, called M1 to M4, are used in the mesh convergence study, with the mesh parameters and total number of elements (n_{total}) summarized in Table 1.

Simulations are performed using a time step $\Delta t = 0.08$, of which the results are shown in Fig. 7a, where the angle θ is plotted as a function of strain, and in Fig. 7b, where the angular velocity of the outer particles ω_z is plotted as a function of strain. Note, that the peaks in angular velocity are due to remeshing, specifically the projection of the old solutions needed for time integration onto the new mesh, and the peaks become smaller on finer meshes. It

16

Table 1: The meshes used in the convergence study. The total number of elements and nodes are approximations, since the meshes change during the simulation.

	n_{part}	n_{min}	number of elements	number of nodes
M1	32	1	~ 5000	~ 8000
M2	64	2	~ 20000	~ 31000
M3	96	3	~ 58000	~ 88000
M4	128	4	~ 188000	~ 272000

can be observed that the angle θ initially increases, an indication that the particles are moving past each other. For mesh M1, θ indeed keeps growing and the particles pass each other. However, for mesh M2, M3 and M4, the angle decreases after going through a maximum and reaches a steady value around $t\dot{\gamma} = 40$. At this point, the particles have formed a stable string, as will be further investigated in the next sections. Since the occurrence of particle alignment is the main subject of this paper, mesh M1 is clearly too coarse (although alignment was observed on meshes similar to M1, but this was very mesh dependent). Furthermore, the angular velocity will be investigated in more detail in this paper, which appears to be accurate on mesh M3. Simulations will thus be performed on mesh M3, which offers a good trade-off between accuracy and efficiency. For the two-particle problem, the same meshing parameters are used (i.e. $n_{\mathrm{part}} = 96$ and $n_{\mathrm{min}} = 3$).

Time convergence is investigated using mesh M3 for three time steps: $\Delta t = 0.08, 0.04$ and 0.02, the results of which are presented in Fig. 7c and Fig. 7d. The time step Δt is normalized by the inverse of the strain rate $\dot{\gamma}^{-1}$. The plots completely overlap for the three values of Δt, indicating that accurate results can be obtained with $\Delta t = 0.08$, which will be the time step used in all subsequent simulations for both the two-particle problem and the three-particle problem.

5.2 Influence of the minimal gap size

As was explained in Section 4.3, a minimal distance between the particle boundaries is introduced, which is denoted by d_{min}. Here, the influence of this parameter on the alignment of the particles is investigated for the three-particle problem. In Fig. 8, results are presented of the angle θ as a function of strain for $\alpha = 0.01$, $\beta = 0.1$ and varying values of Wi. Several sets of results are shown for $d_{\mathrm{min}} = 0.08, 0.04, 0.02$ and 0.01. For $d_{\mathrm{min}} = 0.08$, particle alignment takes
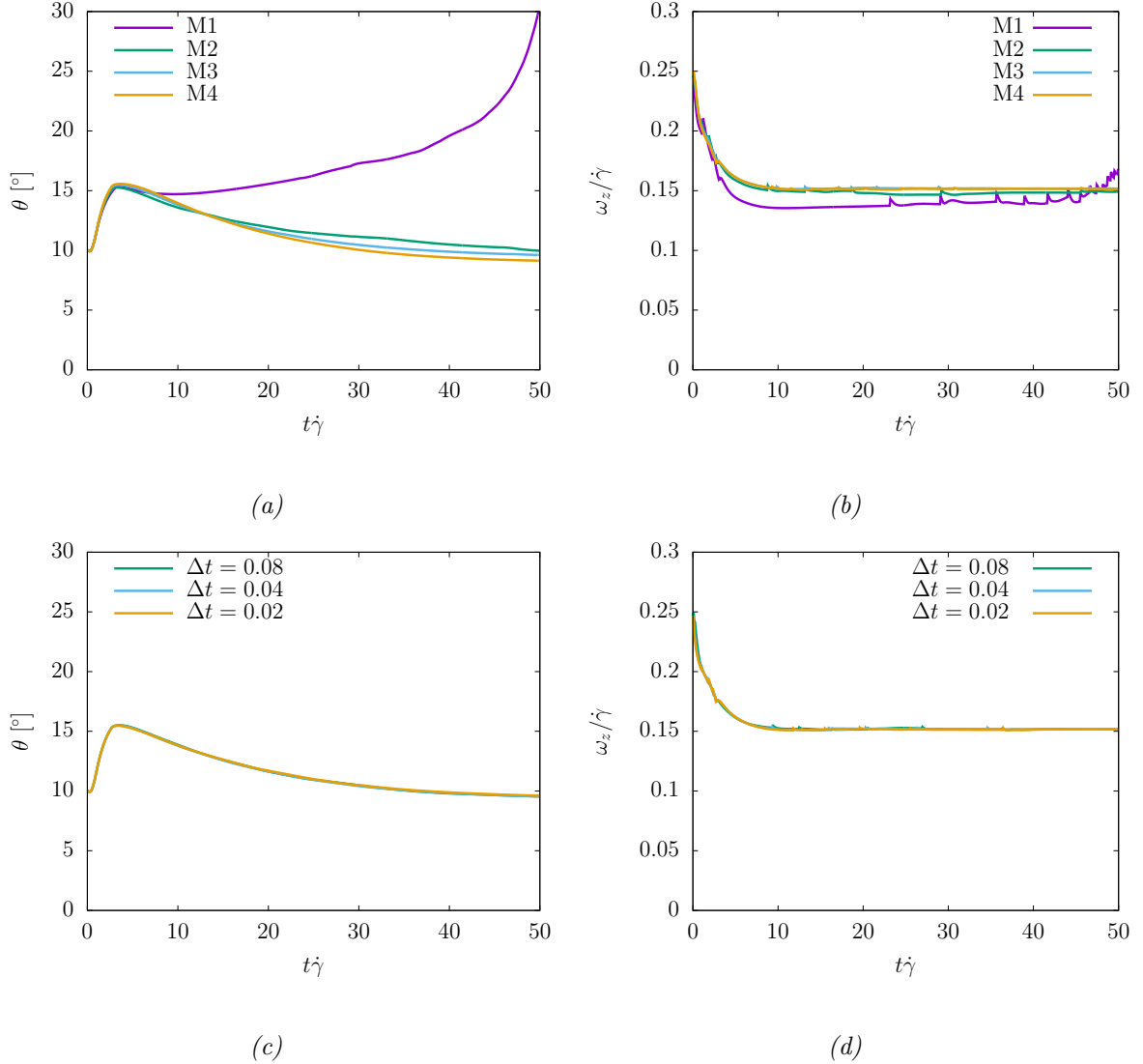
Fig. 7: Mesh convergence of the angle θ (a) and the angular velocity ω_z of the outer particles (b) and time convergence of the angle θ (c) and the angular velocity ω_z of the outer particles (d). Here Wi = 3, $\alpha = 0.01$, $\beta = 0.1$, $d_{\min} = 0.02$ *and three particles are simulated.*

place for Wi ≥ 2. For $d_{\min} = 0.04$, particle alignment is observed for Wi ≥ 2.5, which is similar to $d_{\min} = 0.02$. For $d_{\min} = 0.01$, particle alignment takes place for Wi ≥ 3. These results indicate that the exact value of Wi for alignment to take place depends on $d_{\min}$, with the transition to alignment being pushed to higher values of Wi when decreasing $d_{\min}$. This raises the question whether alignment will still occur for $d_{\min} = 0$. However, setting $d_{\min} = 0$ results in very large deformation rates in the gaps between the particles. As a result, large polymer stresses are generated, leading to a breakdown of the numerical scheme. For particles with a diameter of 2.7 μm (similar to the polystyrene spheres used in [29]), setting $d_{\min} = 0.01$ corresponds to a

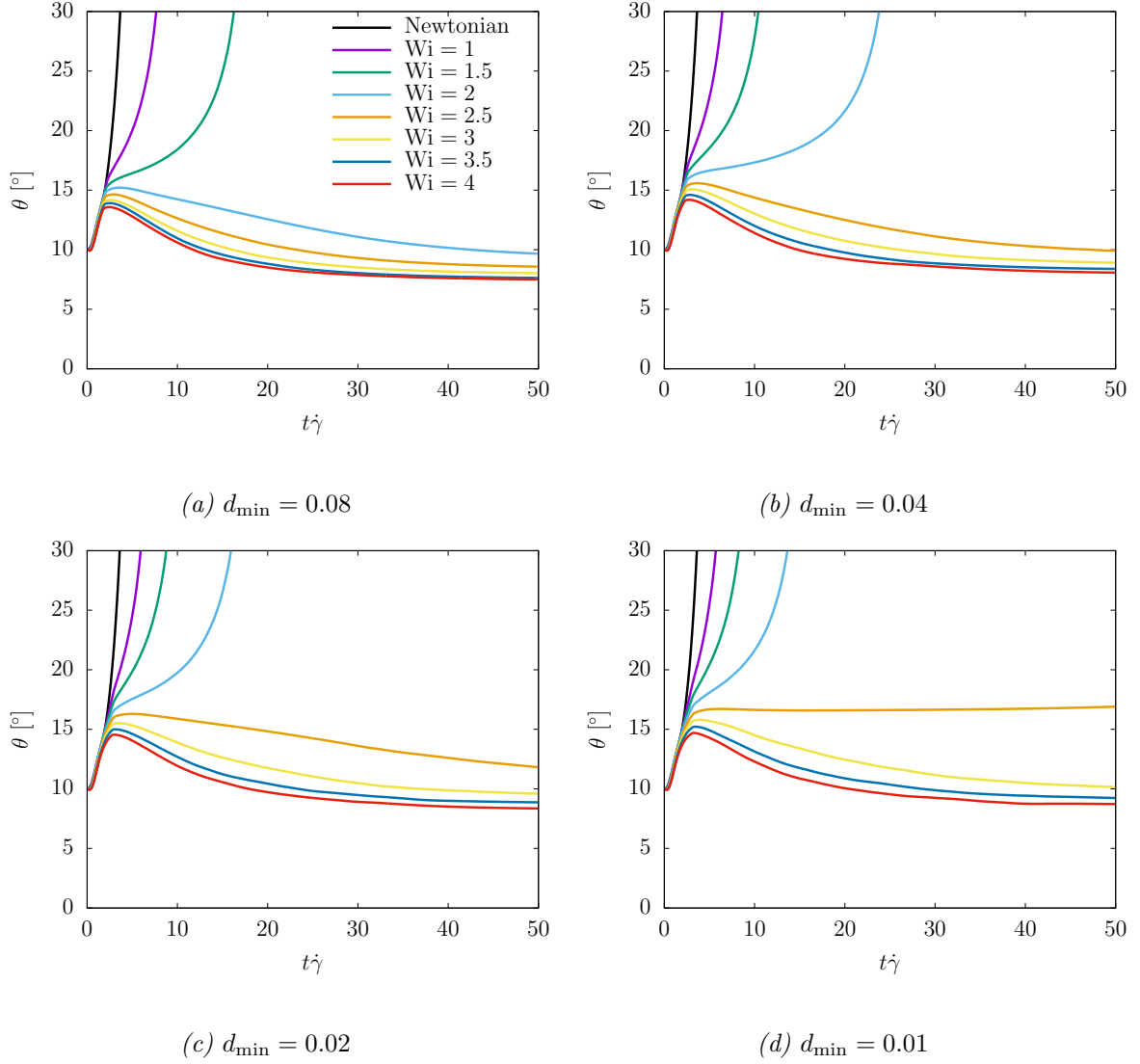*(a) $d_{\min} = 0.08$*

(b) $d_{\min} = 0.04$

(c) $d_{\min} = 0.02$

(d) $d_{\min} = 0.01$

Fig. 8: The angle θ as a function of strain for $\alpha = 0.01$ and $\beta = 0.1$ and varying Wi *for the three-particle problem. The minimal distance is set to $d_{\min} = 0.08$ (a), $d_{\min} = 0.04$ (b), $d_{\min} = 0.02$ (a), and $d_{\min} = 0.01$ (d).*

particle roughness of about 27 nm. We will use $d_{\min} = 0.02$ in all subsequent simulations, and the detailed analysis of the influence of a minimal distance between the particles will be subject of future research.

Having verified the accuracy of our numerical technique and the influence of the parameter $d_{\min}$, we will now continue with the analysis of particle alignment, paying specific attention to the rheology of the suspending fluid.

5.3 Alignment in viscoelastic fluids

In this section, we will investigate the alignment of two and three particles in a suspending fluid with $\alpha = 0.1$, $\beta = 0.1$ in more detail. With these fluid parameters, the alignment occurs at similar Wi for two and three particles, which allows for comparison between the simulations of two particles and three particles. In all subsequent simulations a minimal distance of $d_{\mathrm{min}} = 0.02$ is used.

5.3.1 Two particles

Simulations of two particles in a suspending fluid with $\alpha = 0.1$ and $\beta = 0.1$ are presented in Fig. 9a, where the angle θ is shown at a function of strain. Alignment clearly takes place at Wi ≥ 1.5, with a final value for θ that decreases with increasing Wi. Note, that alignment of two isolated particles was not observed in the experiments by Snijkers et al. [45], but was later observed in experiments at higher shear rate by van Loon et al. [2].

The magnitude of the repulsive force F_{r} (needed to maintain the minimal gap size) and particle rotation ω_z are shown in Fig. 9b and 9c, respectively. The angular velocities of the two particles are equal (with very slight deviations due to the asymmetry of the mesh), thus only one angular velocity is shown. Furthermore, the force F_{r} is scaled with $F_{\mathrm{S}} = 6\pi a^2 \dot{\gamma} \eta_0$, which is the Stokes' drag of a particle moving through a viscous fluid of viscosity η_0 at a velocity $a\dot{\gamma}$. A positive value for F_{r} means that the force is repulsive. Furthermore, the angular velocity is scaled with $\dot{\gamma}$, which yields a value of 0.5 for an isolated spherical particle in a Newtonian fluid [46]. As the particles align, the repulsive force goes to a constant value, which decreases with increasing Wi, which might be attributed to the lower viscosity at higher Wi in the shear-thinning Giesekus fluid. However, comparing F_{r} for different Wi is difficult, since the angle θ is not the same for all Wi. For higher values of θ the particles is located in a region with higher absolute values of the velocity due to the imposed shear, thus a larger repulsive force is needed to keep the particles apart.

Also the angular velocity shows a decrease with increasing Wi, similarly to what was observed in simulations and experiment on an isolated sphere [47, 48]. As was mentioned by Hwang and Hulsen [20], the angular velocity plays a large role in string formation, and a reduction of about 60% with respect to the angular velocity of a particle suspended in a Newtonian fluid was

observed. Michele et al. [1] observed an almost vanishing angular velocity of particles in strings. Van Loon et al. [2] mention that the existence of a fluid film in between the particles is essential due to the particles being able to rotate and thus satisfy the zero-torque condition individually, instead of tumbling with the complete chain.
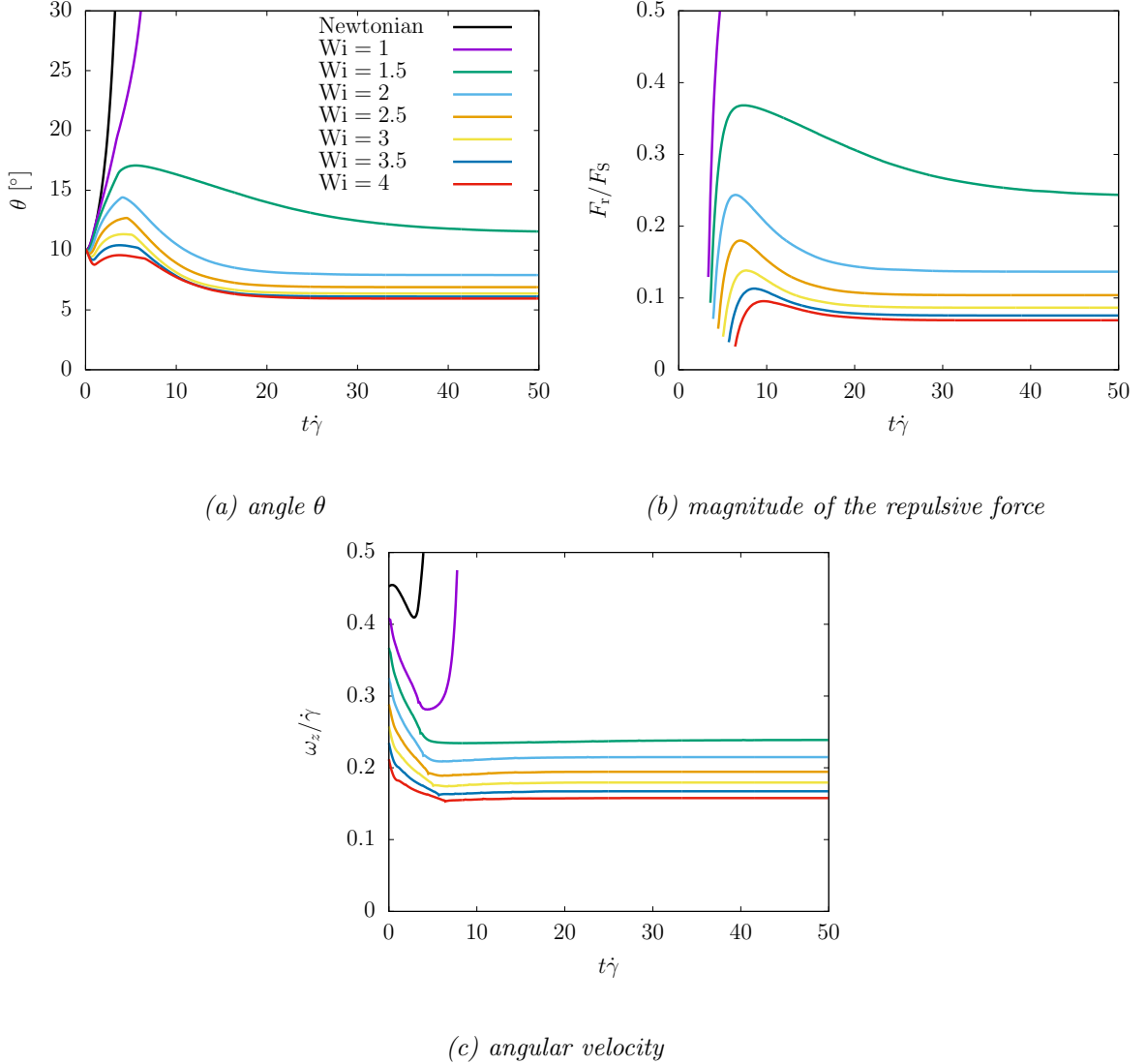

(a) angle θ

(b) magnitude of the repulsive force

(c) angular velocity

Fig. 9: The angle θ (a), repulsive force F_r (b) and angular velocity ω_z (c) as a function of strain. Two particles are simulated in a suspending fluid with $\alpha = 0.1$, $\beta = 0.1$ and varying Wi.

In Fig. 10 the trace of the polymer stress tensor is shown in the case of two aligning particles (Wi = 3, $\alpha = 0.1$ and $\beta = 0.1$). At $t\dot{\gamma} = 0$, polymer stresses are observed which are due to the $\boldsymbol{c}_0$ used, as explained in Section 3.1. At $t\dot{\gamma} = 8$, the particles have moved close to each other and the polymer stress field has changed significantly. Regions of high polymer stress are observed in the gap between the particles, where there exist high local shear rates due to the rotation

21

of the particles. Furthermore, an asymmetric distribution of stresses around the particles can be observed, with regions of high stress above the right particle and below the left particle. At $t\dot\gamma = 16$, a steady situation has been reached, and hardly any difference is observed with the conformation field and orientation of the particles at $t\dot\gamma = 48$. The particles align with a slight angle with respect to the x-axis.
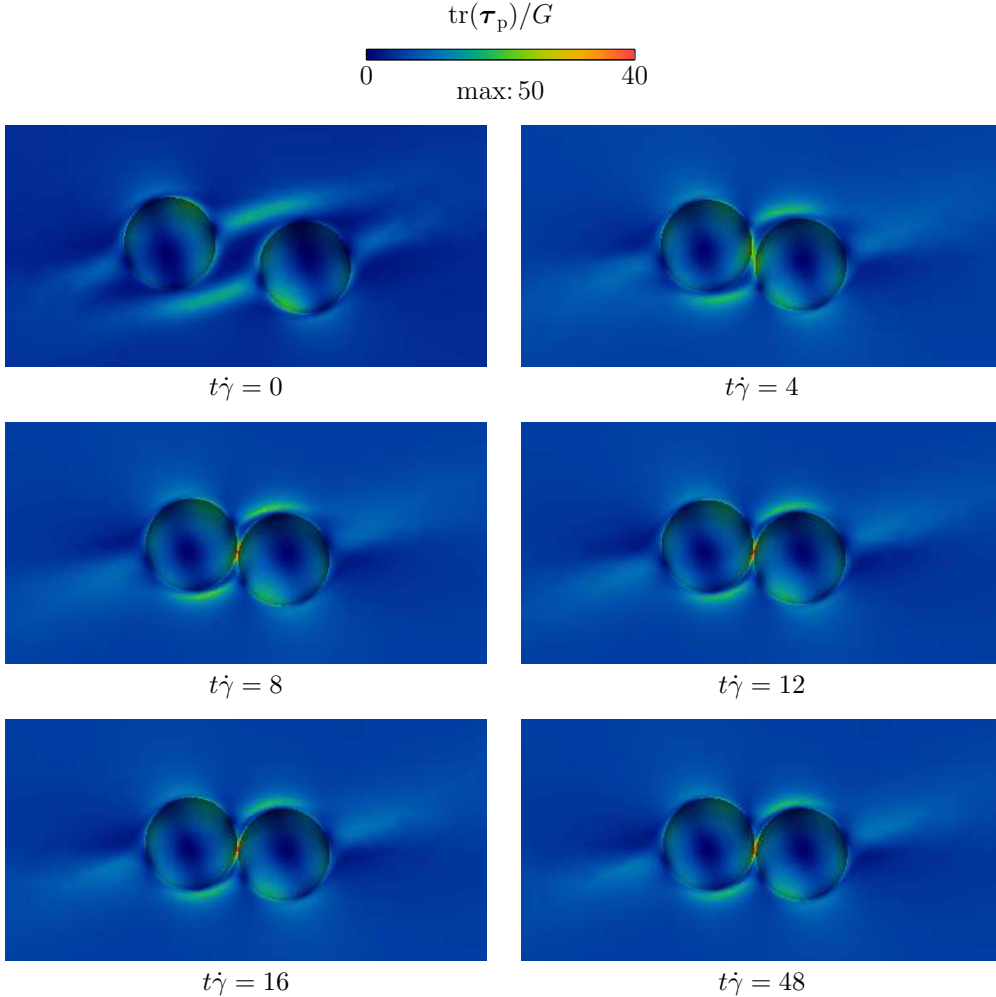

Fig. 10: *Snapshots of the polymer stress during alignment of two particles* (Wi $= 3$, $\alpha = 0.1$ *and* $\beta = 0.1$). *A close-up of the polymer stress at $t\dot\gamma = 48$ is shown in Fig. 13a.*

5.3.2 Three particles

Simulations of three particles in a suspending fluid with $\alpha = 0.1$ and $\beta = 0.1$ are presented in Fig. 11a, where the angle θ is shown as a function of strain. Similar to two particles, alignment takes place at Wi ≥ 1.5, but the final values of θ are smaller than for the two-particle simulations. This is an indication that the alignment of three particles occurs more readily (at lower Wi)

than the alignment of two particles, which will be shown to be indeed the case in Section 5.4.

The magnitude of the repulsive force is shown in Fig. 11b, which is about a factor two smaller than for the case of two particles. However, a direct comparison is again difficult due to the different values of θ. The angular velocity of the middle and outer particles are shown in Fig. 11c and 11d, respectively. For all Wi, an initial decrease of the angular velocity is observed as the particles move toward each other. For particles that do not align (Wi $\leq$ 1), the angular velocity goes through a minimum and increases again as the particles move around each other. For particles that do align (Wi $\geq$ 1.5), the particle angular velocity decreases and reaches a steady value around $t\dot{\gamma} = 10$. The final value of the angular velocity depends on Wi: higher values of Wi lead to lower values of the angular velocity. The trends are equal for the inner and outer particles, but the middle particle rotates significantly slower. This can be explained by the middle particle experiencing resistance from the two outer particles, whereas the outer particles only experience resistance from the single middle particle. Interestingly, the angular velocity in the two-particle problem is similar to the angular velocity of the outer particles in the three-particle problems. Due to the slower rotation of the middle particle (and the gap between the particles being equal) the deformation rates in between the particles are lower for three particles than for two particles. Therefore, the normal stresses in the gap between the particles are lower, which might explain why three particles align more readily.

In Fig. 12 the trace of the polymer stress tensor is shown in the case of three aligning particles (Wi = 3, $\alpha = 0.1$ and $\beta = 0.1$). Initially, larger polymer stresses are observed when compared to the two aligning particles shown in Fig. 10. Furthermore, regions of large polymer stresses are observed around the middle particle, which appear to contribute to the stresses around the outer particles. This contribution of the middle particle to the stresses around the outer particles offers another explanation as to why three particles align at lower Wi for the same α and β (as will be shown in Section 5.4). Close to steady state, the string retains an angle with respect to the x-axis, as can be seen at $t\dot{\gamma} = 48$. Finally, we present a comparison of the polymer stress in the gap between the particles for the two- and three-particle problems in Fig. 13. Indeed, the stresses in the gap are lower for the three-particle problem, which can be attributed to the angular velocity of the middle particle being lower, as was shown in Fig. 11.
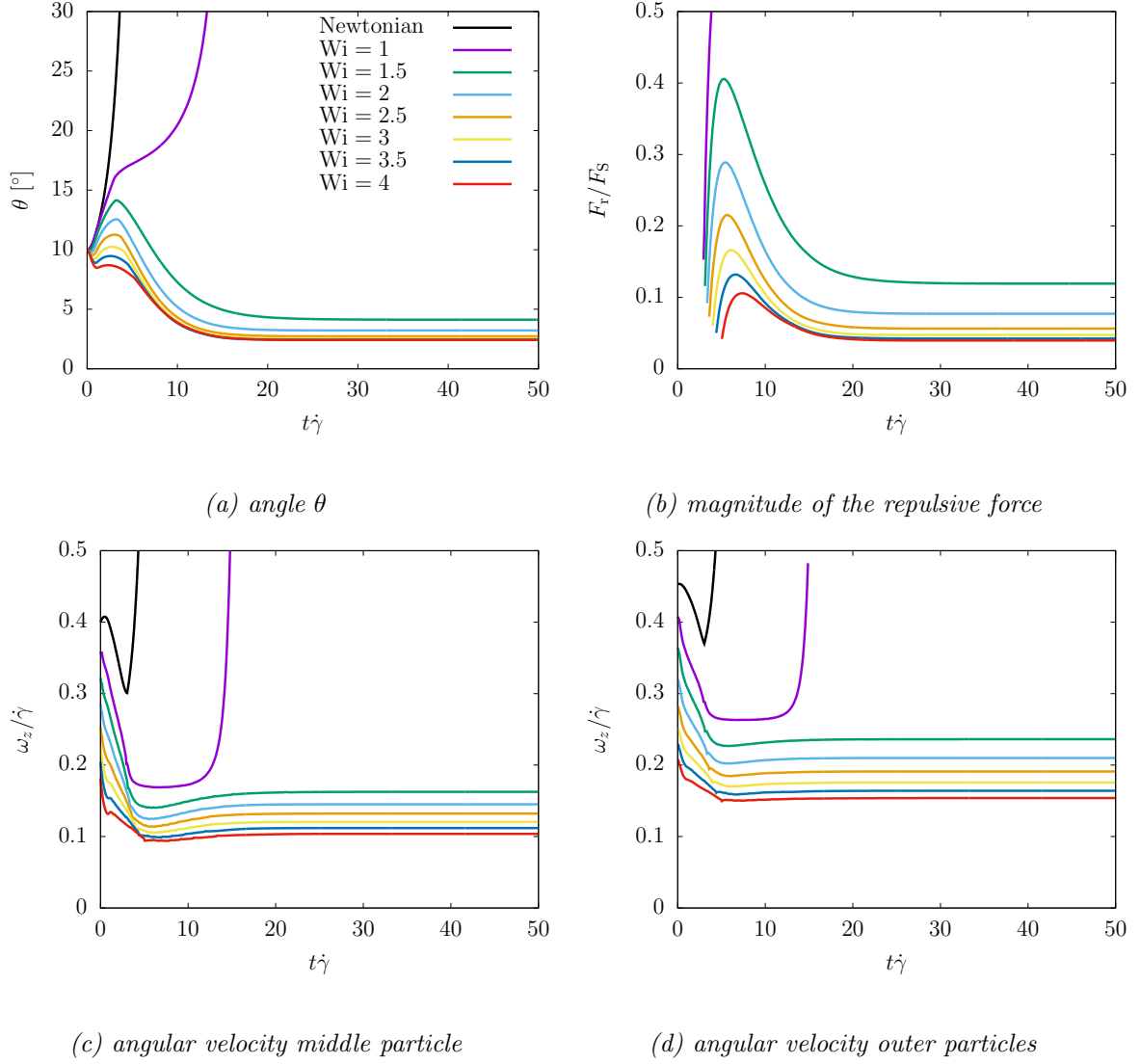
(a) angle θ

(b) magnitude of the repulsive force

(c) angular velocity middle particle

(d) angular velocity outer particles

Fig. 11: The angle θ (a), repulsive force F_r (b) and angular velocities ω_z of the middle (c) and outer (d) particles as a function of strain. Three particles are simulated in a suspending fluid with $\alpha = 0.1$, $\beta = 0.1$ and varying Wi.

5.4 Morphology diagrams

Next, the influence of the rheology of the suspending fluid is investigated. As was shown by Hwang and Hulsen [20], it is more appropriate to analyze alignment in terms of the elasticity parameter S of the suspending fluid, which is defined by

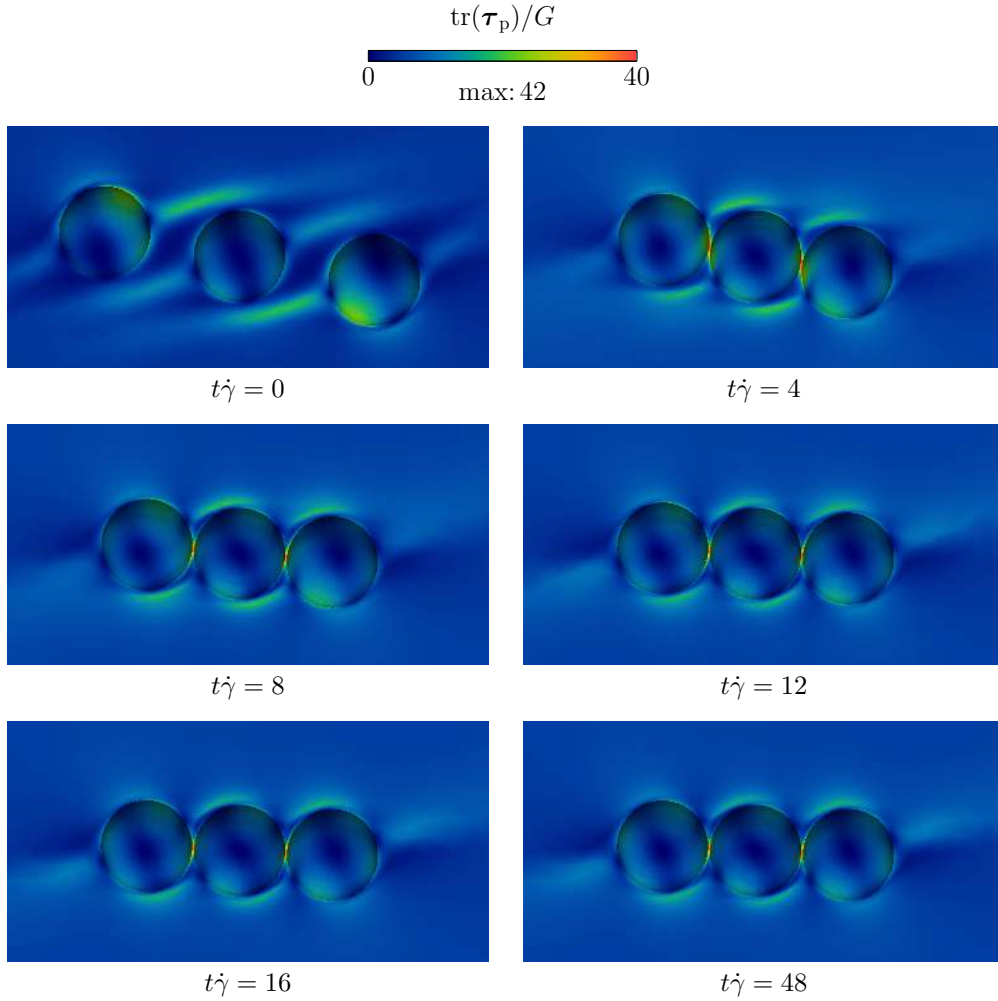$$S = \frac{1}{2}\frac{N_1}{\sigma_{xy}}, \tag{33}$$

24

Fig. 12: Snapshots of the polymer stress during alignment of three particles (Wi = 3, α = 0.1 *and* β = 0.1). *A close-up of the polymer stress at* $t\dot{\gamma} = 48$ *is shown in Fig. 13b.*

where N_1 is the steady first normal stress difference and σ_{xy} is the shear stress of the pure fluid in simple shear. The relationship between S and Wi is shown in Fig. 14 for several values of α and β. The curve goes through a maximum which depends on both α and β: above a certain value of Wi, increasing Wi further leads to a decrease of the elasticity parameter. To investigate the influence of the Weissenberg number, shear thinning and solvent viscosity, many simulations were performed for varying Wi, α and β for both the two-particle and the three-particle problem. By evaluating curves such as the angle θ versus $t\dot{\gamma}$, it can be deduced if the particles are aligning in a string or passing each other. If the angle θ is constant or decreasing at $t\dot{\gamma} = 50$, we will assume that the particles have aligned in a stable string.

In this manner, morphology plots can be created as is shown in Fig. 15 for two particles and in Fig. 16 for three particles. For constant α and β, three particles align at lower Wi

$\text{tr}(\boldsymbol{\tau}_{\mathrm{p}})/G$
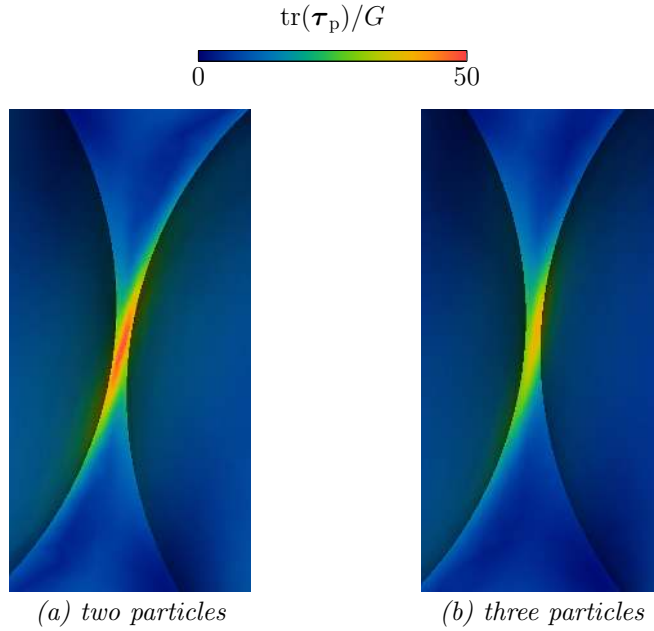
0   50

(a) two particles   (b) three particles

Fig. 13: Close-up of the polymer stress in the gap between the particles at $t\dot\gamma = 48$ for two particles (a) and three particles (b) ($\text{Wi} = 3$, $\alpha = 0.1$ and $\beta = 0.1$).

than two particles. Possible explanations given in Section 5.3 were that the middle particle rotates more slowly in the three particles problem (yielding lower normal stresses in the fluid film between the particles), or the middle particle contributing to the stresses around the outer particles. The morphology plots indicate that S indeed plays a large role in particle alignment. Alignment appears to occur above a certain critical value of S, which varies with α: for lower values of alpha, a higher S is needed for alignment. As can be seen in Fig. 14, the value of S goes through a maximum for increasing Wi. From this, one would expect that when Wi is increased, alignment would stop occurring at some point. The simulations of two particles at $\alpha = 0.2$ and $\beta = 0.2$ presented in Fig. 15c and three particles at $\alpha = 0.2$ and $\beta = 0.3$ presented in Fig. 16c show this is indeed the case. For the two-particle problem, no alignment is observed for $\beta \geq 0.3$, whereas for the three particle problem, no alignment is observed for $\beta \geq 0.4$.

These results are in agreement with the literature, where shear-thinning was observed to play a crucial role in alignment [2]. Extrapolating the results to large values of β, typical for Boger fluids (e.g. a two-mode Giesekus fit to the rheological data of a Boger fluid yielded $\beta = 0.56$ in [49]), yields large values of Wi needed for alignment, which might explain why alignment is not observed in Boger fluids. Moreover, the results indicate that the critical value for S for alignment to occur increases for decreasing α. This critical value of S might not be reached

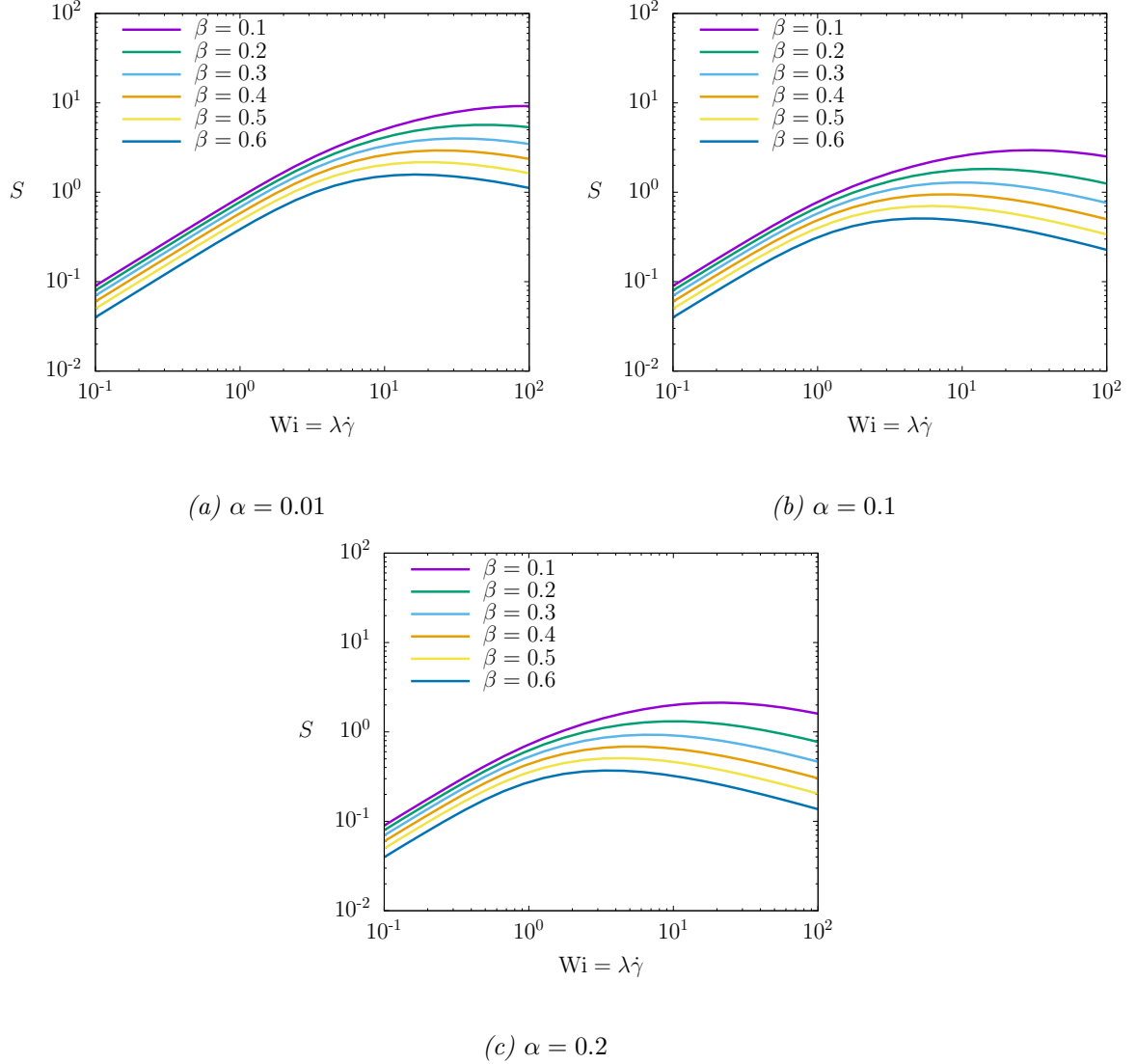(a) $\alpha = 0.01$

(b) $\alpha = 0.1$

(c) $\alpha = 0.2$

Fig. 14: The elasticity parameter S as a function of Wi for the pure fluid for $\alpha = 0.01$ (a), $\alpha = 0.1$ (b) and $\alpha = 0.2$ (c) (simple shear).

in experiments or might not even be reachable at all (i.e. for values of α that are not zero, S has a maximum as shown in Fig. 14). A similar observation was done by Hwang and Hulsen, although their problem was 2D, with biperiodic boundary conditions [20].

The simulations we have presented up until now are in agreement with the literature: alignment occurs in fluids that are both elastic and shear thinning. Although alignment was observed for a weakly shear-thinning fluid ($\alpha = 0.01$), an interesting case is $\alpha = 0$, thus a constant viscosity, elastic Oldroyd-B fluid. Simulations of three particles were performed for $\alpha = 0$ and $\beta = 0.1$, but mesh-convergence and stability were much more difficult to obtain. Preliminary results (not shown here) indicate that for Wi ≥ 6, the particles align. A value of Wi $= 6$

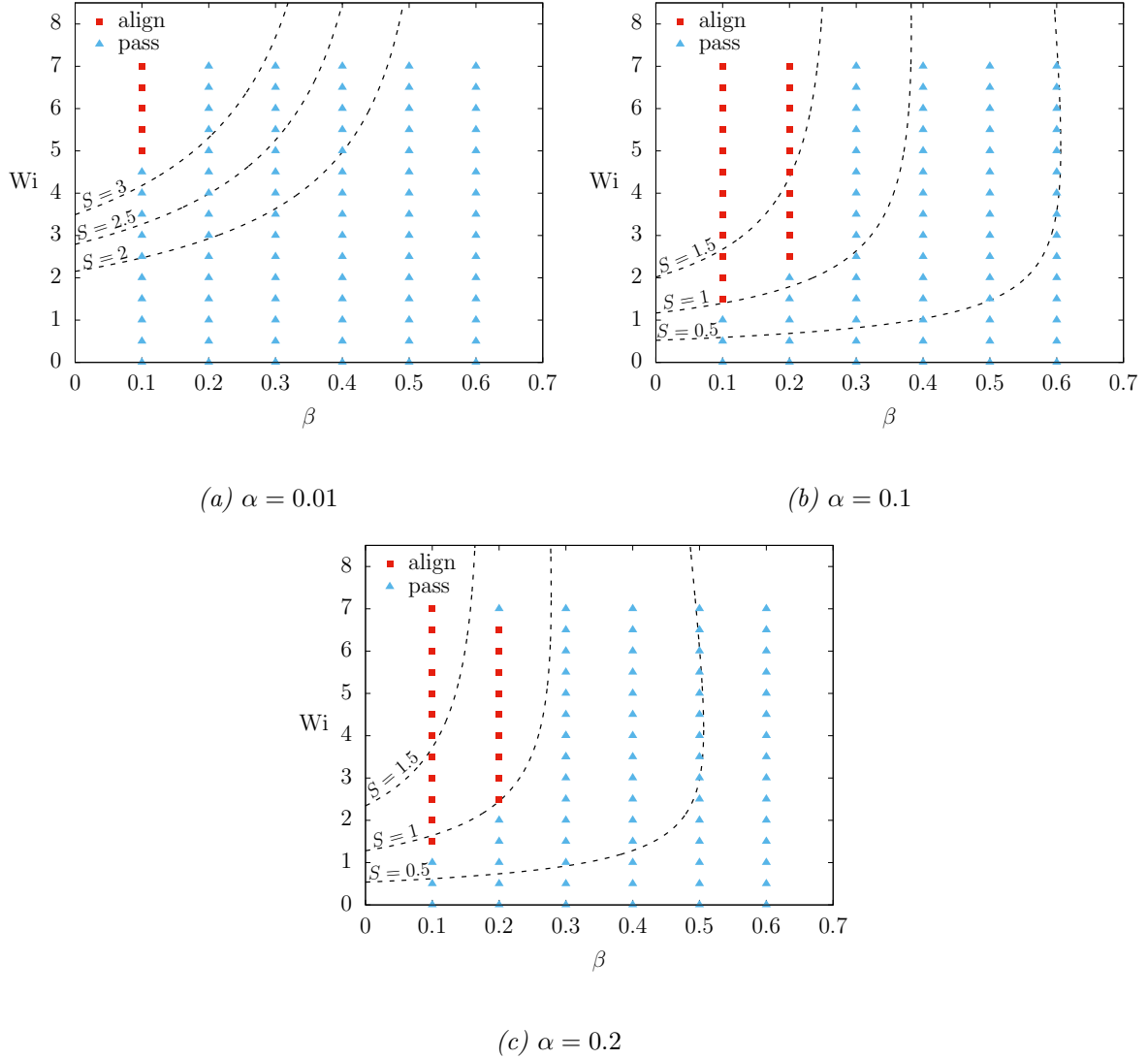*(a) $\alpha = 0.01$* *(b) $\alpha = 0.1$*

(c) $\alpha = 0.2$

Fig. 15: Morphology plots describing the alignment or passing of two particles for $\alpha = 0.01$ (a), $\alpha = 0.1$ (b) and $\alpha = 0.2$ (c) for varying combinations of Wi and β. Isolines for constant values of the elasticity parameter S are plotted as well.

corresponds to $S = 5.4$ (for an Oldroyd-B fluid $S = (1 - \beta)$Wi). These results indicate that shear-thinning is not needed for particle alignment, although it was shown to have a strong alignment-promoting effect. This is in contrast with the experimental results presented in [2]. In the next section, we will study particles suspended in non-elastic shear-thinning fluids.

5.5   Non-elastic shear-thinning fluids

For generalized Newtonian fluids, alignment is not to be expected. This follows from a simple argument given by Phillips [50]: the momentum balance Eq. (1), together with the Cauchy

(a) $\alpha = 0.01$

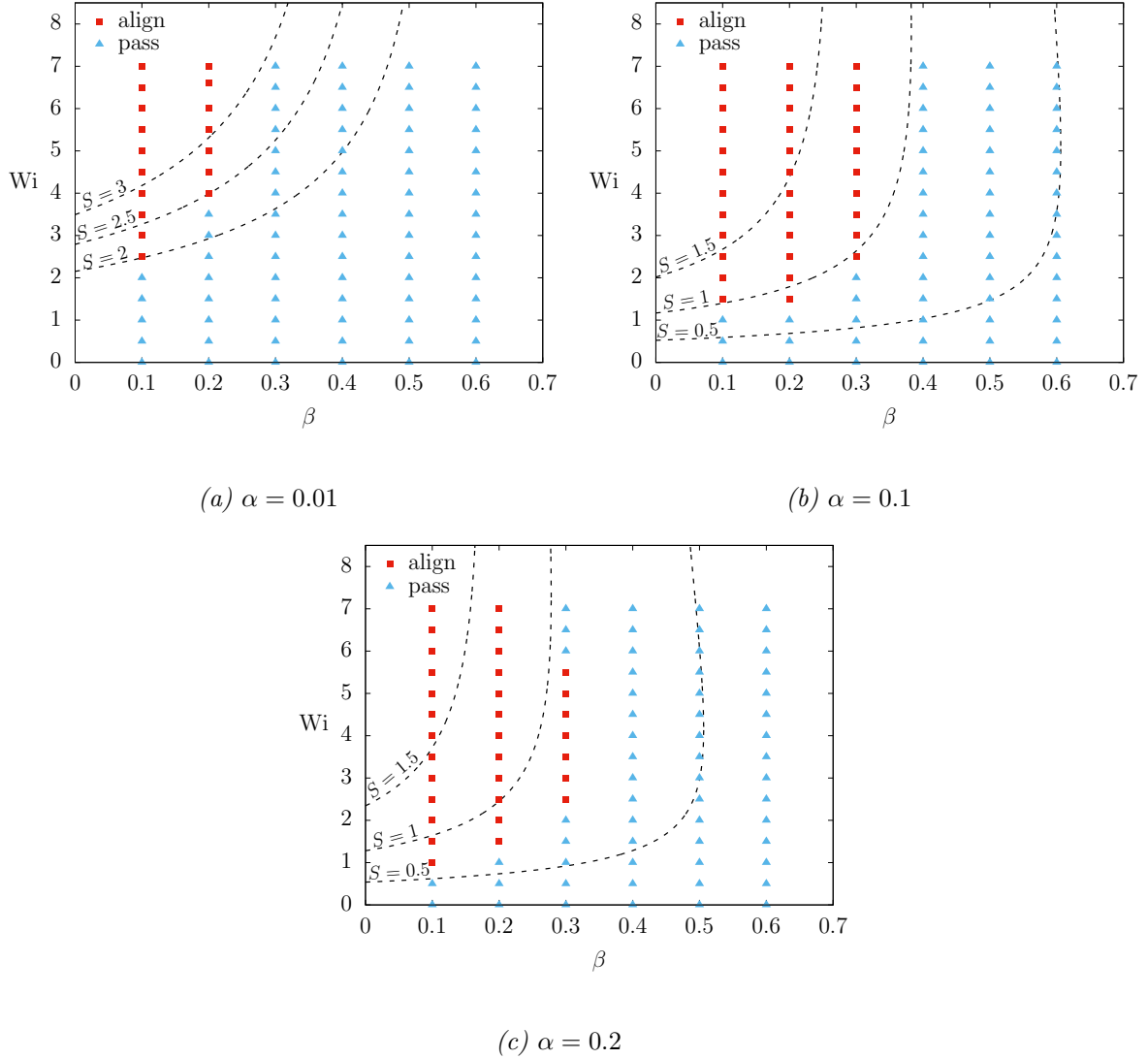*(b) $\alpha = 0.1$*

(c) $\alpha = 0.2$

Fig. 16: Morphology plots describing the alignment or passing of three particles for $\alpha = 0.01$ (a), $\alpha = 0.1$ (b) and $\alpha = 0.2$ (c) for varying combinations of Wi and β. Isolines for constant values of the elasticity parameter S are plotted as well.

stress given by Eq. (8), is non-linear but reversible in time (i.e. upon flow reversal, the velocities, pressures and viscous stresses change signs). If the flow is reversed, the particles would thus trace back their paths, and any structure that was formed during flow would be lost. This leads to a paradox: for a generalized Newtonian fluid, reversing the flow does not alter the physical picture since the viscosity is an instantaneous function of the strain rate and does not depend on the direction of the velocity. The only conclusion is thus that alignment cannot take place in generalized Newtonian fluids. We should emphasize that in the simulations presented in this paper, irreversibility is introduced by enforcing a minimal distance between the particles (see

Section 4.3), which yields a repulsive force that does not change sign upon flow reversal. To investigate the effect of the shear-thinning on the interaction between the particles, we will now move on to non-elastic shear-thinning fluids, described by the Carreau model (Eq. (9)). The dimensionless groups describing the problem are $\lambda_c\dot{\gamma}$ and the power-law index n. In Fig. 17 the shear viscosity of the pure fluid is shown for a strongly thinning fluid ($n = 0.1$), weakly thinning fluid ($n = 0.7$) and two intermediate cases ($n = 0.3$ and $n = 0.57$). The fluid with $n = 0.57$ is chosen such that the power-law index is equal to the power-law index of the shear-thinning fluid used by van Loon et al. [2], where particle strings were observed. The initial force on the particles, which is released in one strain unit (see Section 3.1), is not necessary in this case.
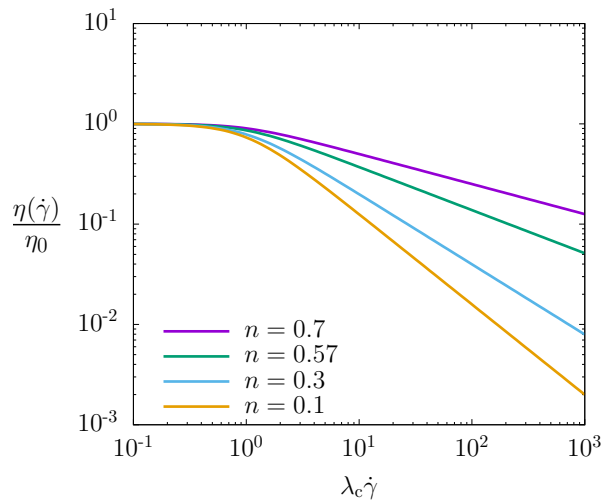

Fig. 17: Shear rate dependent viscosity of the Carreau fluid for varying values of n (simple shear).

5.5.1 Three particles

Simulations are performed at $\lambda_c\dot{\gamma} = 1, 10$ and 100 for the three-particle problem. The results of the angle θ as a function of strain are shown in Fig. 18. In none of the simulations in purely shear-thinning fluids, the particles reach a steady location with respect to each other, i.e. no alignment is observed. For $\lambda_c\dot{\gamma} = 10$ and $\lambda_c\dot{\gamma} = 100$, the results are similar: which is most likely due to the imposed shear rate already being in the shear-thinning part of the viscosity curve as shown in Fig. 17. For $\lambda_c\dot{\gamma} = 1$, the results are different, with the particles passing each other more rapidly. In this case, the imposed shear rate is close to the Newtonian plateau, whereas the shear rate in between the particles is further down the shear-thinning part of the curve. For all values of $\lambda_c\dot{\gamma}$, the particle trajectories are affected by the amount of shear-thinning in

the suspending fluid: when decreasing the power-law index n, it takes longer for the particles to move around each other.

To conclude, we present the angular velocity and magnitude of the repulsive force (scaled by $F_{\mathrm{S}} = 6\pi a^2 \dot{\gamma} \eta_0$, see Section 5.3) in Fig. 19. For both the middle particle and the outer particles, the angular velocity is larger for smaller values of n in the initial part of the simulation. Around $t\dot{\gamma} = 3$, the particle movement is constrained and a discontinuity in the angular velocities for the Carreau fluids can be observed. This can be explained by a sudden decrease in effective shear-rate (and thus an increase in viscosity) as the particles stop moving toward each other. The Newtonian curve shows a kink, but it is continuous. In the second part of the simulation, where the particle movement is constrained, the angular velocity is smaller for smaller values of n, which is opposite to the initial part of the simulation. The trends of the angular velocity are similar for the middle particle and the outer particles, but the angular velocity for the middle particle is slightly lower, due to the middle particle experiencing resistance from the two outer particles. The repulsive force is shown in Fig. 19c, where a decrease of F_{r} is observed with increased shear-thinning. We attribute this effect to an effective decrease of the viscosity around and between the particles, yielding lower viscous stresses and thus a smaller repulsive force.

5.5.2 Two particles

We have performed simulations for two particles in the same non-elastic shear-thinning Carreau fluids as used in the previous section. No alignment was observed, and the results are comparable to the three-particle problem and will thus not be reproduced here.
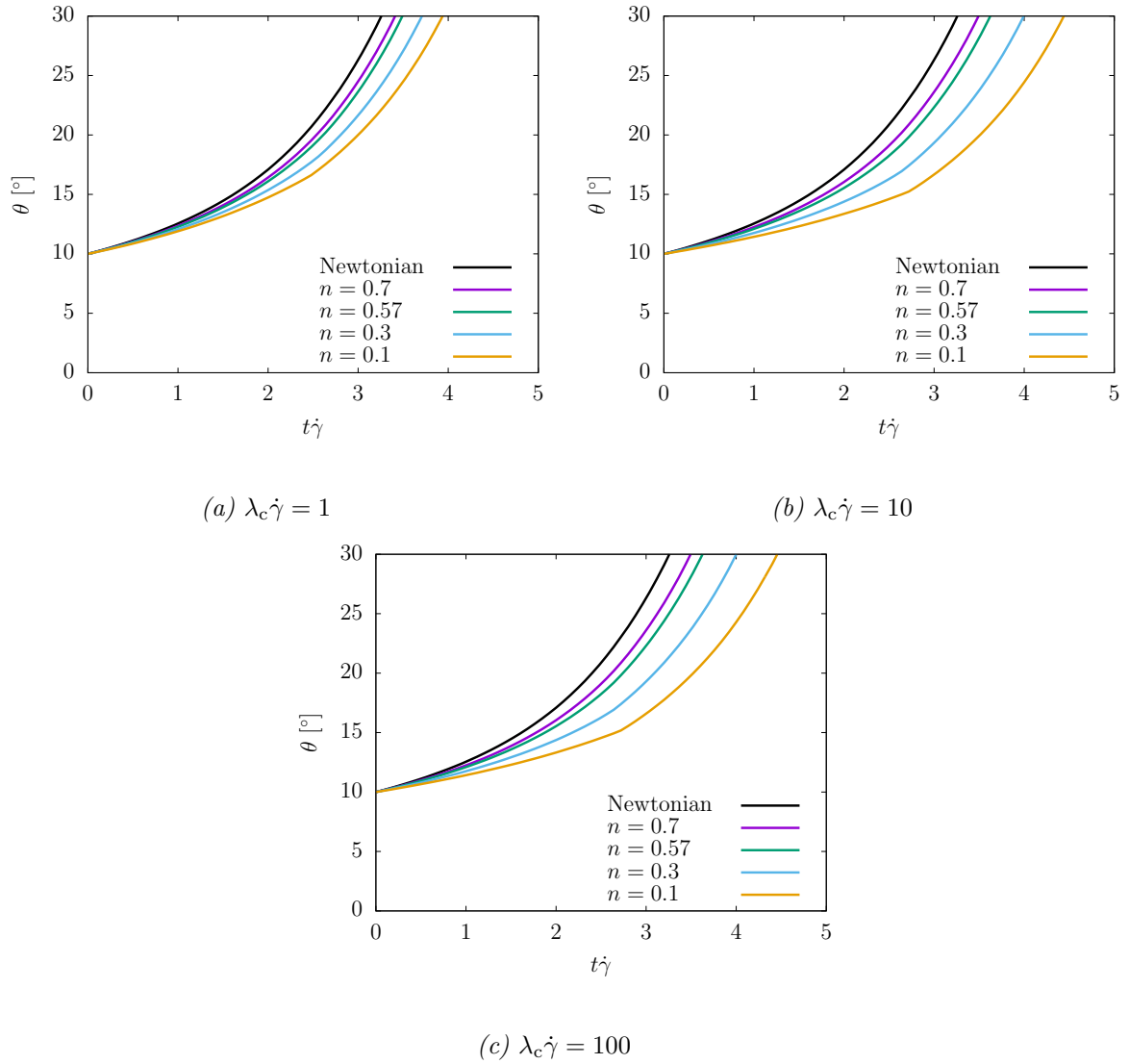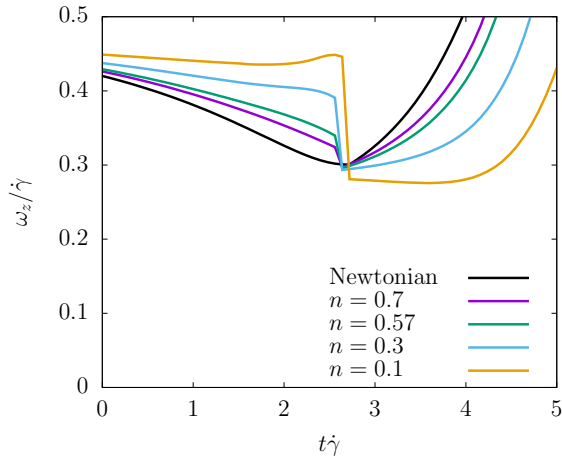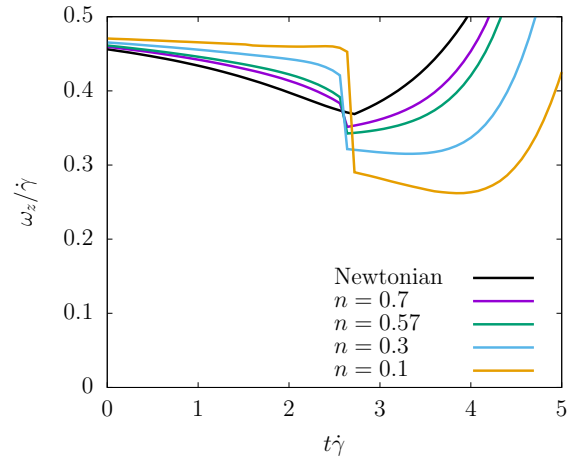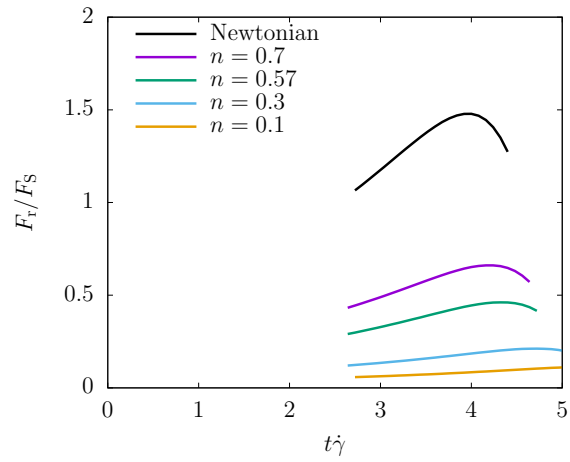
(a) $\lambda_c \dot{\gamma} = 1$

(b) $\lambda_c \dot{\gamma} = 10$

(c) $\lambda_c \dot{\gamma} = 100$

Fig. 18: The angle θ as a function of strain in a Carreau fluid for $\lambda_c \dot{\gamma} = 1$ (a), $\lambda_c \dot{\gamma} = 10$ (b) and $\lambda_c \dot{\gamma} = 100$ (c).

32

(a) angular velocity middle particle

(b) angular velocity outer particles

(c) magnitude of the repulsive force

Fig. 19: The angular velocity of the middle particle (a), outer particle (b) and magnitude of the repulsive force as a function of strain (c) in a Carreau fluid for $\lambda_c \dot{\gamma} = 10$.

6 Discussion and conclusion

We have presented the first 3D direct numerical simulations of particle alignment in viscoelastic fluids. The influence of the rheology of the suspending fluid, specifically its shear-thinning behavior, the Weissenberg number and the solvent viscosity ratio, was investigated for the alignment of two and three particles. Accurately describing the polymer stress in the fluid was found to be essential for the formation of particle strings, and mesh-dependent results were obtained on coarse meshes. Due to the use of adaptive meshing, the resolution around the particles can be locally increased to obtain mesh-independent results.

A fluid film in between the particles is essential such that they can satisfy the zero-torque condition individually, instead of tumbling as a whole [2]. As opposed to the 2D simulations presented in [18, 20], the particles come into close proximity to each other in the 3D case, yielding very large deformation rates in the gaps between the particles. As a result, large polymer stresses are generated, leading to a breakdown of the numerical scheme. This problem was solved by introducing a small minimal gap size. This minimal gap size is implemented as a constraint, thus the repulsive force follows from the Lagrange multipliers and does not have to be specified a-priori. Alignment was observed for a minimal gap size of 1% of the particle diameter. However, increasing the minimal gap size appears to promote alignment. This raises the question whether alignment will still occur if the minimal gap size goes to zero since no evidence was found that a fluid film of constant thickness develops between the particles. This is consistent with experiments presented by van Loon et al. [2], where the use of a depletion force (effectively lowering $d_{\min}$) was shown to hinder particle alignment. In the simulations, however, this film might be much thinner than in the 2D case, due to the interaction between spheres occurring over smaller surfaces. A possible explanation for the existence of a repulsive force is particle roughness [37]. For particles with a diameter of 2.7 μm (similar to the polystyrene spheres used in [29]), a value for $d_{\min}$ of 1% of the particle diameter corresponds to roughness of about 27 nm.

The alignment of particles appears to be strongly dependent on the ratio between the first normal stress difference and the shear stress of the suspending fluid, expressed in the "elasticity parameter" S. For fluids where $S = 0$, i.e. non-elastic shear-thinning fluids, no alignment is observed. For viscoelastic fluids, alignment occurs above a certain value of S, which is lower for

a more shear thinning fluid, whereas the presence of a solvent viscosity makes it more difficult for particles to align. The use of S to describe alignment is supported by simulations that indicate that alignment stops occurring above a certain value of Wi, which can be explained by S going through a maximum for increasing Wi (for $\alpha > 0$). Extrapolating the results to large values of the solvent viscosity, typical for Boger fluids, might explain why particles do not align in Boger fluids: the value of S for alignment to occur is very high and might not be reached in experiments or might not even be reachable at all (i.e. for values of α that are not zero, S has a maximum as shown in Fig. 14). This does, however, not explain why alignment occurs in shear-thinning fluids without significant normal stress differences [2]. A possible explanation might be that the (small) normal stress differences present in this fluid are responsible for the alignment. Also, the presence of other particles might promote alignment, as was observed in the 2D simulations presented in [21].

Supported by the lack of alignment in non-elastic shear-thinning fluids and the results of particle alignment in weakly shear-thinning fluids, we conclude that normal stress differences are essential for particle alignment to occur, whereas shear-thinning can have a strong alignment-promoting effect. However, an elaborate comparison of experimental and numerical results, especially with respect to the existence of a fluid film in between the particles, is necessary to validate the numerical model presented in this paper. This will be topic of future research.

Acknowledgment

References

[1] J. Michele, R. Pätzold, and R. Donis. Alignment and aggregation effects in suspensions of spheres in non-Newtonian media. *Rheologica Acta*, 16:317–321, 1977.

[2] S. Van Loon, J. Fransaer, C. Clasen, and J. Vermant. String formation in sheared suspensions in rheologically complex media: The essential role of shear thinning. *Journal of Rheology*, 58(1):237–254, 2014.

[3] A. Einstein. Eine neue Bestimmung der Moleküldimensionen. *Annalen der Physik*, 19:289–306, 1906.

[4] A. Einstein. Berichtigung zu meiner Arbeit: Eine neue Bestimmung der Moleküldimensionen. *Annalen der Physik*, 34:591–592, 1911.

[5] M.M. Denn and J.F. Morris. Rheology of non-Brownian suspensions. *Annual Review of Chemical and Biomolecular Engineering*, 5:203–28, 2014.

[6] J. Mewis and N.J. Wagner. Current trends in suspension rheology. *Journal of Non-Newtonian Fluid Mechanics*, 157:147–150, 2009.

[7] A. Sierou and J.F. Brady. Rheology and microstructure in concentrated noncolloidal suspensions. *Journal of Rheology*, 46(5):1031–1056, 2002.

[8] F. Boyer, E. Guazzelli, and O. Pouliquen. Unifying suspension and granular rheology. *Physical Review Letters*, 107:188301, 2011.

[9] R. Mari, R. Seto, J.F. Morris, and M.M. Denn. Shear thickening, frictionless and frictional rheologies in non-Brownian suspensions. *Journal of Rheology*, 58(6):1693–1724, 2014.

[10] S.Y. Fu, X.Q. Feng, B. Lauke, and Y.W. Mai. Effects of particle size, particle/matrix interface adhesion and particle loading on mechanical properties of particulate-polymer composites. *Composites Part B: Engineering*, 39:933–961, 2008.

[11] G. D'Avino and P.L. Maffettone. Particle dynamics in viscoelastic liquids. *Journal of Non-Newtonian Fluid Mechanics*, 215:80–104, 2015.

[12] M.A. Tehrani. An experimental study of particle migration in pipe flow of viscoelastic fluids. *Journal of Rheology*, 40(6):1057–1077, 1996.

[13] G. D'Avino, T. Tuccillo, P.L. Maffettone, F. Greco, and M.A. Hulsen. Numerical simulations of particle migration in a viscoelastic fluid subjected to shear flow. *Computers and Fluids*, 39:709–721, 2010.

[14] G. D'Avino, F. Snijkers, R. Pasquino, M. A. Hulsen, F. Greco, P. L. Maffettone, and J. Vermant. Migration of a sphere suspended in viscoelastic liquids in Couette flow: experiments and simulations. *Rheologica Acta*, 51(3):215–234, 2012.

[15] M.K. Lyon, D.W. Mead, R.E. Elliott, and L.G. Leal. Structure formation in moderately concentrated viscoelastic suspensions in simple shear flow. *Journal of Rheology*, 45(4):881–890, 2001.

[16] R. Pasquino, D. Panariello, and N. Grizzuti. Migration and alignment of spherical particles in sheared viscoelastic suspensions. A quantitative determination of the flow-induced self-assembly kinetics. *Journal of Colloid and Interface Science*, 394:49–54, 2013.

[17] D.D. Joseph and J.J. Feng. A note on the forces that move particles in a second-order fluid. *Journal of Non-Newtonian Fluid Mechanics*, 64:299–302, 1996.

[18] Y.J. Choi and M.A. Hulsen. Alignment of particles in a confined shear flow of a viscoelastic fluid. *Journal of Non-Newtonian Fluid Mechanics*, 175-176:89–103, 2012.

[19] R. Pasquino, G. D'Avino, P.L. Maffettone, F. Greco, and N. Grizzuti. Migration and chaining of noncolloidal spheres suspended in a sheared viscoelastic medium. Experiments and numerical simulations. *Journal of Non-Newtonian Fluid Mechanics*, 203:1–8, 2014.

[20] W.R. Hwang and M.A. Hulsen. Structure formation of non-colloidal particles in viscoelastic fluids subjected to simple shear flow. *Macromolecular Materials and Engineering*, 296:321–330, 2011.

[21] N.O. Jaensson, M.A. Hulsen, and P.D. Anderson. Simulations of the start-up of shear flow of 2D particle suspensions in viscoelastic fluids: structure formation and rheology. *Journal of Non-Newtonian Fluid Mechanics*, 225:70–85, 2015.

[22] I.S. Santos de Oliveira, A. van den Noort, J.T. Padding, W.K. den Otter, and W.J. Briels. Alignment of particles in sheared viscoelastic fluids. *Journal of Chemical Physics*, 135:104902, 2011.

[23] I.S. Santos de Oliveira, W.K. den Otter, and W.J. Briels. Alignment and segregation of bidisperse colloids in a shear-thinning viscoelastic fluid under shear flow. *Europhysics Letters*, 101:28002, 2013.

[24] G. D'Avino, F. Greco, M.A. Hulsen, and P.L. Maffetone. Rheology of viscoelastic suspensions of spheres under small and large amplitude oscillatory shear by numerical simulations. *Journal of Rheology*, 57(3):813–839, 2013.

[25] S. Yoon, M.A. Walkley, and O.G. Harlen. Two particle interactions in a confined viscoelastic fluid under shear. *Journal of Non-Newtonian Fluid Mechanics*, 185-186:39–48, 2012.

[26] M. Yang, S. Krishnan, and E.S.G. Shaqfeh. Numerical simulations of the rheology of suspensions of rigid spheres at low volume fraction in a viscoelastic fluid under shear. *Journal of Non-Newtonian Fluid Mechanics*, 234:51–68, 2016.

[27] G Li, G.H. McKinley, and A.M. Ardekani. Dynamics of particle migration in channel flow of viscoelastic fluids. *Journal of Fluid Mechanics*, 785:486–505, 2015.

[28] D. Won and C. Kim. Alignment and aggregation of spherical particles in viscoelastic fluid under shear flow. *Journal of Non-Newtonian Fluid Mechanics*, 117:141–146, 2004.

[29] R. Scirocco, J. Vermant, and J. Mewis. Effect of the viscoelasticity of the suspending fluid on structure formation in suspensions. *Journal of Non-Newtonian Fluid Mechanics*, 117:183–192, 2004.

[30] C. Geuzaine and J.-F. Remacle. Gmsh: A 3D finite element mesh generator with built-in pre- and post-processing facilities. *International Journal for Numerical Methods in Engineering*, 79(11):1309–1331, 2009.

[31] H. Giesekus. A simple constitutive equation for polymer fluids based on the concept of deformation-dependent tensorial mobility. *Journal of Non-Newtonian Fluid Mechanics*, 11:69–109, 1982.

[32] G. D'Avino, G. Cicale, M.A. Hulsen, F. Greco, and P.L. Maffettone. Effects of confinement on the motion of a single sphere in a sheared viscoelastic liquid. *Journal of Non-Newtonian Fluid Mechanics*, 157:101–107, 2009.

[33] R. Glowinski, T.-W. Pan, T.I. Hesla, and D.D. Joseph. A distributed Lagrange multiplier/fictitious domain method for particulate flows. *International Journal of Multiphase Flow*, 25:755–794, 1999.

[34] G. D'Avino and M.A. Hulsen. Decoupled second-order transient schemes for the flow of viscoelastic fluids without a viscous solvent contribution. *Journal of Non-Newtonian Fluid Mechanics*, 165:1602–1612, 2010.

[35] M.A. Hulsen, R. Fattal, and R. Kupferman. Flow of viscoelastic fluids past a cylinder at high Weissenberg number: stabilized simulations using matrix logarithms. *Journal of Non-Newtonian Fluid Mechanics*, 127:27–39, 2005.

[36] A.N. Brooks and T.J.R. Hughes. Streamline upwind/Petrov-Galerkin formulations for convection dominated flows with particular emphasis on the incompressible Navier-Stokes equations. *Computational Methods in Applied Mechanical Engineering*, 32:199–259, 1982.

[37] H.H. Hu, N.A. Patankar, and M.Y. Zhu. Direct numerical simulations of fluid-solid systems using the arbitrary Lagrangian-Eulerian technique. *Journal of Computational Physics*, 169:427–462, 2001.

[38] N.O. Jaensson, M.A. Hulsen, and P.D. Anderson. Stokes-Cahn-Hilliard formulations and simulations of two-phase flows with suspended rigid particles. *Computers and Fluids*, 111:1–17, 2015.

[39] R. Fattal and R. Kupferman. Constitutive laws for the matrix-logarithm of the conformation tensor. *Journal of Non-Newtonian Fluid Mechanics*, 123:281–285, 2004.

[40] F.P.T. Baaijens. Mixed finite element methods for viscoelastic flow analysis: a review. *Journal of Non-Newtonian Fluid Mechanics*, 79:361–385, 1998.

[41] HSL. *A collection of Fortran codes for large scale scientific computation*, 2013. `http://www.hsl.rl.ac.uk`.

[42] Y. Saad. *SPARSKIT: A Basic Tool Kit for Sparse Matrix Computations.* NASA Ames Research Center, Moffett Field, CA, Technical Report 2090, 2001.

[43] G. Karypis and V. Kumar. A fast and high quality multilevel scheme for partitioning irregular graphs. *SIAM Journal on Scientific Computing*, 20(1):359–392, 1998.

[44] B. Maury. Direct simulations of 2D fluid-particle flows in biperiodic domains. *Journal of Computational Physics*, 156:325–351, 1999.

[45] F. Snijkers, R. Pasquino, and J. Vermant. Hydrodynamic interactions between two equally sized spheres in viscoelastic fluids in shear flow. *Langmuir*, 29:5701–5713, 2013.

[46] G.B. Jeffery. The motion of ellipsoidal particles immersed in a viscous fluid. *Proceedings of the Royal Society A: Mathematical, Physical and Engineering Sciences*, 102(715):161–179, 1922.

[47] G. D'Avino, M.A. Hulsen, F. Snijkers, J. Vermant, F. Greco, and P.L. Maffettone. Rotation of a sphere in a viscoelastic liquid subjected to shear flow. Part I. Simulation results. *Journal of Rheology*, 52(6):1331–1346, 2008.

[48] F. Snijkers, G. D'Avino, P.L. Maffettone, F. Greco, M.A. Hulsen, and J. Vermant. Rotation of a sphere in a viscoelastic liquid subjected to shear flow. Part II. Experimental results. *Journal of Rheology*, 53(2):459–480, 2009.

[49] F. Snijkers, G. D'Avino, P.L. Maffettone, F. Greco, M.A. Hulsen, and J. Vermant. Effect of viscoelasticity on the rotation of a sphere in shear flow. *Journal of Non-Newtonian Fluid Mechanics*, 166:363–372, 2011.

[50] R.J. Phillips. Structural instability in the sedimentation of particulate suspensions through viscoelastic fluids. *Journal of Non-Newtonian Fluid Mechanics*, 165:479–488, 2010.